Model-Based Levitation Control of A 100 kW Bearingless Electric Motor

Subhadyuti Sahoo

School of Electrical Engineering

Thesis submitted for examination for the degree of Master of Science in Technology.

Espoo (Finland), 26.11.2018

Supervisor

Docent Kai Zenger

Advisor

Dr Rafal Jastrzebski

Aalto University
School of Electrical
Engineering

Aalto University
School of Electrical
Engineering

Aalto University, P.O. BOX 11000, 00076 AALTO
www.aalto.fi
Abstract of the master's thesis

Author Subhadyuti Sahoo

Title Model-Based Levitation Control of A 100 kW Bearingless Electric Motor

Degree programme Automation and Electrical Engineering

Major Control, Robotics and Autonomous Systems **Code of major** ELEC3025

Supervisor Docent Kai Zenger

Advisor Dr Rafal Jastrzebski

Date 26.11.2018 **Number of pages** 12+62 **Language** English

Abstract

The use of magnetically levitated rotors for various applications, especially in pumps and compressors, has seen an unprecedented rise in the last few years. Bearingless motors combine levitation and torque production capabilities. They offer more compact footprint and require less power electronics compared to more traditional active magnetic bearing supported motors. A lot of significance has been attached to reducing cost, complexity and broadening applicability of the magnetically levitated rotors. Hence, the levitation control of rotors in such bearingless machines has become quite an interesting topic of research. Digital control strategies need to be adopted for proper levitation control of rotors. Furthermore, it has to be kept in mind that these rotors cannot afford to have too many oscillations under different environmental conditions because oscillations can eventually lead to instability and heavy losses.

This thesis presents a state-of-the-art model-based digital control of the levitation of a 100 kW bearingless electric motor where the point-mass of the rotor is considered. This motor has a rated speed of 22000 rpm. The entire bearingless motor system is converted into state-space models by taking into account the bearingless machine's nominal operating points and conditions. Then, a model-based controller with Pincer's conditions, coupled with an estimator with Kalman filtering, integral action and state-command path, is implemented and tested for the levitation control. FEM derived Simulink model of the bearingless motor is tested to verify the proposed control strategies. The closed-loop poles and zeroes, step responses of the closed-loop system and the frequency responses are also recorded from the simulations. In the end, the control of the rotor is investigated with five different combinations involving controller, estimator, integrator and state-command path. Comparisons are conducted on the the proposed control strategies and conclusions are drawn based on the findings.

Keywords Bearingless machine, Levitation control, Model-based control, DLQR controller, Kalman filtering, Error integral, State-command, Frequency responses

Preface

At the very beginning, I will express my gratitude towards my entire family, immediate and extended, for their constant love, support, motivation and prayers for me for the entire duration of my Master's studies. This thesis would never have been completed had they not stood by my side, through thick and thin.
I want to thank Docent Kai Zenger, my thesis supervisor, from Aalto University for his valuable suggestions related to my research work. It has indeed been my honour to get him as my supervisor. His lessons on control theory and engineering, in general, and on model-based control systems, in particular, was very helpful for this research work of mine.
I shall also like to extend my thanks to Dr Rafal Jastrzebski, my advisor, from Lappeenranta University of Technology for his tireless and exceptionally patient guidance throughout my research work. His ideas and comments on my progress can neither be estimated nor delineated in words.
Furthermore, I would also like to thank all my friends from Aalto University, my colleagues from Lappeenrantra University of Technology and all my friends from my native nation for providing me the constant motivation and support I needed during the entire length of this research work.

Espoo (Finland), 26.11.2018

Subhadyuti Sahoo

Contents

Abstract ii

Preface iii

Contents iv

Symbols and Abbreviations v

1 Introduction 1
- 1.1 Background . . . 1
- 1.2 Previous Works . . . 1
- 1.3 Objectives of Thesis . . . 1
- 1.4 Outline of Thesis . . . 2

2 Bearingless Systems 4
- 2.1 Applications . . . 4
- 2.2 Modelling of Bearingless Motor . . . 4
- 2.3 Flux Linkages and Winding Currents . . . 4
- 2.4 Suspension Forces . . . 7
- 2.5 State-Space Models . . . 10
  - 2.5.1 Model Structure . . . 10
  - 2.5.2 State-Space Matrices . . . 10
  - 2.5.3 Per-Unit Matrices . . . 11
  - 2.5.4 Discretization . . . 14

3 Linear Quadratic Controller 17
- 3.1 Controller Only . . . 17
- 3.2 Controller with State-command Path . . . 24

4 Kalman Estimator 32
- 4.1 Controller and Estimator . . . 32
- 4.2 Controller with State-command Path and Estimator . . . 41

5 Error Integral 48

6 Stable Control Strategies 56
- 6.1 Comparison of the Two Stable Controllers . . . 56
- 6.2 Ultimate Selection . . . 56

7 Conclusions 58

References 60

Symbols and Abbreviations

Symbols

a_{cc}	translational acceleration
a_g	air gap
$\mathbf{A}$	State matrix
$\mathbf{A}^{\mathrm{T}}$	Transpose of state matrix
$\mathbf{A}_{\mathrm{pu}}$	Per unit state matrix
$\mathbf{B}$	Input-to-State matrix
$\mathbf{B}^{\mathrm{T}}$	Transpose of input-to-state matrix
$\mathbf{B}_{\mathrm{pu}}$	Per unit input-to-state matrix
$\mathbf{C}$	State-to-output Matrix
$\mathbf{C}_{\mathrm{pu}}$	Per unit state-to-output matrix
d_{i}	Input disturbance
d_{o}	Output disturbance
$d_{\mathrm{o}} \rightarrow \mathbf{y}_{\mathrm{out}}$	Output-disturbance-to-Output sensitivity
$\mathbf{D}$	Feedthrough matrix
$\mathbf{D}_{\mathrm{pu}}$	Per unit feedthrough matrix
$\mathbf{e}_k$	Steady state error vector at k^{th} instant
F	Suspension force
F_x	Suspension force in x-axis
F_y	Suspension force in y-axis
$\mathbf{F}$	Discretized state matrix
$\mathbf{F}_{\mathrm{c}}$	Discrete state matrix for system fitted with controller and estimator
g_a	Acceleration due to gravity
$\mathbf{G}$	Discretized input-to-state matrix
$\mathbf{G}_{\mathrm{n}}$	Process-to-state noise matrix
$\mathbf{H}$	State-to-Output matrix used to compute DLQR controller, estimator and integrator matrices
$\mathbf{H}_{\mathrm{n}}$	Process-to-measurement noise matrix
i_{m}	Current in motor windings
$i_{\mathrm{m}d}$	Current in motor d-axis winding
$i_{\mathrm{m}d}^{rms}$	RMS value of current in motor d-axis winding
$i_{\mathrm{m}q}$	Current in motor q-axis winding
$i_{\mathrm{m}q}^{rms}$	RMS value of current in motor q-axis winding
i_{s}	Current in suspension windings
$i_{\mathrm{s}d}$	Current in suspension d-axis winding
$i_{\mathrm{s}d}^{rms}$	RMS value of current in suspension d-axis winding
$i_{\mathrm{s}q}$	Current in suspension q-axis winding
$i_{\mathrm{s}q}^{rms}$	RMS value of current in suspension q-axis winding
$\mathbf{I}$	Identity matrix (of appropriate order(s))
J	Cost function of Riccati equation for controller
k_{x1}	First position stiffness

Symbols (contd...)

k_{x2}	Second position stiffness
$\mathbf{K}$	Controller matrix
$\mathbf{K}_{\mathrm{I}}$	Integrator matrix
L_d	d-axis self-inductance
L_q	q-axis self-inductance
$\mathbf{L}$	Estimator matrix
m	Point mass of rotor
$M_d^{'}$	Suspension force constant in d-axis
$M_q^{'}$	Suspension force constant in q-axis
$\mathbf{N}$	Reduced state-command matrix
$\mathbf{N}_{\mathrm{u}}$	State-command matrix from reference to input
$\mathbf{N}_{\mathrm{x}}$	State-command matrix from reference to state
$\mathbf{O}$	Zero matrix (of appropriate order(s))
$\mathbf{P}$	Solution of discrete Riccati equation for Kalman estimator
$\mathbf{Q}$	Weight matrix on states, used for computing DLQR controller, estimator and integrator matrices
$\overline{\mathbf{Q}}$	Co-weight matrix on states, used for computing DLQR controller, estimator and integrator matrices
$\mathbf{r}_k$	Reference vector for ideal levitated positions
$\mathbf{r}_k \rightarrow \mathbf{e}_k$	Reference-to-Error sensitivity
$\mathbf{R}$	Weight matrix on inputs, used for computing controller, estimator and integrator matrices
$\mathbf{R}_v$	Measurement noise co-variance matrix used for computing Kalman estimator matrix
$\mathbf{R}_w$	Process noise co-variance matrix used for computing Kalman estimator matrix
$\mathbf{R}_{wv}$	Process-measurement noise co-variance matrix
$\mathbf{S}$	Infinite horizon solution of discrete Riccati equation for controller
T_s	Sampling period
$\mathbf{T}_{\mathrm{x}}$	Per unit transformation matrix for states
$\mathbf{T}_{\mathrm{x}}^{-1}$	Inverse of per unit transformation matrix for states
$\mathbf{T}_{\mathrm{u}}$	Per unit transformation matrix for inputs
$\mathbf{T}_{\mathrm{u}}^{-1}$	Inverse of per unit transformation matrix for inputs
$\mathbf{T}_{\mathrm{yout}}$	Per unit transformation matrix for outputs
$\mathbf{T}_{\mathrm{yout}}^{-1}$	Inverse of per unit transformation matrix for outputs
u_1	First input to the system
u_2	Second input to the system
$\mathbf{u}$	Input vector
$\mathbf{u}_{grav}$	Input vector containing terms related to gravitational forces
$\mathbf{u}_k$	Discretized input vector at k^{th} instant
$\mathbf{u}_k^{\mathrm{T}}$	Transpose of discretized input vector at k^{th} instant
$\mathbf{u}_{nl}$	Coupled input vector
$\mathbf{u}_{\mathrm{pu}}$	Per unit input vector
W_m	Stored magnetic energy
$W_m^{'}$	Stored magnetic co-energy

Symbols (contd...)

$\mathbf{W}_\mathrm{c}$	Controllability matrix
$\mathbf{W}_\mathrm{o}$	Observability matrix
x	Displacement in x-axis
x_lim	Limit of displacement in x-axis
x_ref	Reference of ideal displacement in x-axis
$\hat{x}$	Estimated displacement in x-axis
$\dot{x}$	Velocity in x-axis
$\ddot{x}$	Acceleration in x-axis
$\mathbf{x}$	State vector
$\mathbf{x}_{\mathrm{I}(k)}$	Steady-state-error-integrated state vector at k^th instant
$\mathbf{x}_{\mathrm{I}(k+1)}$	Steady-state-error-integrated state vector at $(k+1)^\mathrm{th}$ instant
$\mathbf{x}_k$	Discretized state vector at k^th instant
$\mathbf{x}_k^\mathrm{T}$	Transpose of discretized state vector at k^th instant
$\mathbf{x}_{k+1}$	Discretized state vector at $(k+1)^\mathrm{th}$ instant
$\mathbf{x}_{nl}$	Coupled state vector
$\mathbf{x}_\mathrm{pu}$	Per unit state vector
$\dot{\mathbf{x}}_\mathrm{pu}$	First order derivative of per unit state vector
$\hat{\mathbf{x}}_k$	Vector containing estimated states of the system at k^th instant
$\hat{\mathbf{x}}_{k+1}$	Vector containing estimated states of the system at $(k+1)^\mathrm{th}$ instant
y	Displacement in y-axis
y_lim	Limit of displacement in y-axis
y_ref	Reference of ideal displacement in y-axis
$\hat{y}$	Estimated displacement in y-axis
$\dot{y}$	Velocity in y-axis
$\ddot{y}$	Acceleration in y-axis
$\mathbf{y}_\mathrm{out}$	Output vector
$\mathbf{y}_{\mathrm{out}k}$	Output vector at k^th instant
$\mathbf{y}_\mathrm{outpu}$	Per unit output vector
λ_m	Flux linkage due to stator magnetic field
$\lambda_\mathrm{m}^{'}$	Current stiffness in Active Magnetic Bearings
$\Psi_{\mathrm{m}d}$	Flux linkage of motor in d-axis winding
$\Psi_{\mathrm{m}q}$	Flux linkage of motor in q-axis winding
$\Psi_{\mathrm{s}d}$	Flux linkage of suspension in d-axis winding
$\Psi_{\mathrm{s}q}$	Flux linkage of suspension in q-axis winding
ω_0	Natural frequency of the system
ω_s	Sampling frequency for discretization of the system

Abbreviations

AMB	Active Magnetic Bearings
CLQC	Continuous Linear Quadratic Controller
dB	decibel(s)
DLQC	Discrete Linear Quadratic Controller
FPGA	Field Programmable Gate Array
KE	Kalman Estimator
LQC	Linear Quadratic Controller
mm	millimeter
MMF	Magneto-Motive Force
PM	Permanent Magnet
PMSM	Permanent Magnet Synchronous Motor
PU	Per Unit
RGA	Relative Gain Array
RMS	Root-Mean-Square
SVD	Singular Value Decomposition

List of Figures

1 **Figure 1**: Winding Arrangements in Rotor Co-Ordinates (left) and Relative Positions of Stator and Rotor during an operation(right)[9] . 5
2 **Figure 2**: Unbalance magnetic pull at no-load and at nominal torque[6] 8
3 **Figure 3**: Forces in x- and y-directions for different i_s and i_m values 8
4 **Figure 4**: $\lambda_m^{'}$ and $M_q^{'}$ for different i_s and i_m values 9
5 **Figure 5**: Pole-Zero Map of the Uncontrolled System 15
6 **Figure 6**: Controlled System's Structure with Controller Only 17
7 **Figure 7**: Pole-Zero Map of the System with Controller 20
8 **Figure 8**: Step Response of the System with Controller 20
9 **Figure 9**: Reference-to-Error Sensitivity (System with controller) . . 21
10 **Figure 10**: Output-disturbance-to-Output Sensitivity (System with Controller) 21
11 **Figure 11**: **(a)** Suspension current waveform in d-axis in absence of q-axis motor current, **(b)** Suspension current waveform in q-axis in absence of q-axis motor current 22
12 **Figure 12**: **(a)** x-axis rotor position responses in absence of q-axis motor current, **(b)** y-axis rotor position responses in absence of q-axis motor current 22
13 **Figure 13**: **(a)** Suspension current waveform in d-axis in presence of q-axis motor current, **(b)** Suspension current waveform in q-axis in presence of q-axis motor current 23
14 **Figure 14**: **(a)** x-axis rotor position responses in presence of q-axis motor current, **(b)** y-axis rotor position responses in presence of q-axis motor current 23
15 **Figure 15**: Controlled System's Structure with Controller and State-command path 24
16 **Figure 16**: Controlled System's Structure with Controller and State-command path (Reduced Form) 24
17 **Figure 17**: Pole-Zero Map of the System with Controller and State-Command path 27
18 **Figure 18**: Step Response of the System with Controller and State-Command path 27
19 **Figure 19**: Reference-to-Error Sensitivity (Controller and State-command path) 28
20 **Figure 20**: Output-Disturbance-to-Output Sensitivity (Controller and State-command path) 28
21 **Figure 21**: Rotor Lift-Up Dynamics (Controller with State-Command) – **(a)** Suspension current waveform in d-axis, **(b)** Suspension current waveform in q-axis, **(c)** x-axis rotor position, **(d)** y-axis rotor position, **(e)** Simulated suspension force waveform along x-axis, **(f)** Simulated suspension force waveform along y-axis 29

22 **Figure 22**: Step Change and Motor Current Dynamics (Controller with State-Command) – **(a)** x-axis rotor position, **(b)** y-axis rotor position, **(c)** Suspension current waveform in d-axis, **(d)** Suspension current waveform in q-axis, **(e)** Simulated suspension force waveform along x-axis, **(f)** Simulated suspension force waveform along y-axis . 30
23 **Figure 23**: Step Input and Output Disturbances Dynamics (Controller with State-Command) – **(a)** x-axis rotor position, **(b)** y-axis rotor position, **(c)** Suspension current waveform in d-axis, **(d)** Suspension current waveform in q-axis, **(e)** Simulated suspension force waveform along x-axis, **(f)** Simulated suspension force waveform along y-axis 31
24 **Figure 24**: Controlled System's Structure with Controller and Estimator 32
25 **Figure 25**: Pole-Zero Map of the System with Controller and Estimator 36
26 **Figure 26**: Step Response of the System with Controller and Estimator 36
27 **Figure 27**: Reference-to-Error Sensitivity (Controller and Estimator) 37
28 **Figure 28**: Output-Disturbances-to-Output Sensitivity (Controller and Estimator) 37
29 **Figure 29**: Rotor Lift-Up Dynamics (Controller and Estimator) – **(a)** Suspension current waveform in d-axis, **(b)** Suspension current waveform in q-axis, **(c)** x-axis rotor position, **(d)** y-axis rotor position, **(e)** Simulated suspension force waveform along x-axis, **(f)** Simulated suspension force waveform along y-axis 38
30 **Figure 30**: Step Change and Motor Current Dynamics (Controller and Estimator) – **(a)** x-axis rotor position, **(b)** y-axis rotor position, **(c)** Suspension current waveform in d-axis, **(d)** Suspension current waveform in q-axis, **(e)** Simulated suspension force waveform along x-axis, **(f)** Simulated suspension force waveform along y-axis 39
31 **Figure 31**: Step Input and Output Disturbances Dynamics (Controller and Estimator) – **(a)** x-axis rotor position, **(b)** y-axis rotor position, **(c)** Suspension current waveform in d-axis, **(d)** Suspension current waveform in q-axis, **(e)** Simulated suspension force waveform along x-axis, **(f)** Simulated suspension force waveform along y-axis . 40
32 **Figure 32**: Controlled System's Structure with Controller, State-command and Estimator 41
33 **Figure 33**: Pole-Zero Map of the System with Controller, State-command Path and Estimator 43
34 **Figure 34**: Step Response of the System with Controller, State-command Path and Estimator 43
35 **Figure 35**: Reference-to-Error Sensitivity (Controller, State-command Path and Estimator) 44
36 **Figure 36**: Output-Disturbances-to-Output Sensitivity (Controller, State-command Path and Estimator) 44

37 **Figure 37**: Rotor Lift-Up Dynamics (Controller, State-command Path and Estimator) – **(a)** Suspension current waveform in d-axis, **(b)** Suspension current waveform in q-axis, **(c)** x-axis rotor position, **(d)** y-axis rotor position, **(e)** Simulated suspension force waveform along x-axis, **(f)** Simulated suspension force waveform along y-axis . 45
38 **Figure 38**: Step Change and Motor Current Dynamics (Controller, State-command Path and Estimator) – **(a)** x-axis rotor position, **(b)** y-axis rotor position, **(c)** Suspension current waveform in d-axis, **(d)** Suspension current waveform in q-axis, **(e)** Simulated suspension force waveform along x-axis, **(f)** Simulated suspension force waveform along y-axis 46
39 **Figure 39**: Step Input and Output Disturbances Dynamics (Controller, State-command Path and Estimator) – **(a)** x-axis rotor position, **(b)** y-axis rotor position, **(c)** Suspension current waveform in d-axis, **(d)** Suspension current waveform in q-axis, **(e)** Simulated suspension force waveform along x-axis, **(f)** Simulated suspension force waveform along y-axis 47
40 **Figure 40**: Controlled System's Structure with Controller, Estimator and Error Integral 48
41 **Figure 41**: Pole-Zero Map of the System with Controller, Estimator and Integration 51
42 **Figure 42**: Step Response of the System with Controller, Estimator and Integration 51
43 **Figure 43**: Reference-to-Error Sensitivity 52
44 **Figure 44**: Output Disturbance-to-Output Sensitivity 52
45 **Figure 45**: Rotor Lift-Up Dynamics – **(a)** Suspension current waveform in d-axis, **(b)** Suspension current waveform in q-axis, **(c)** x-axis rotor position, **(d)** y-axis rotor position, **(e)** Simulated suspension force waveform along x-axis, **(f)** Simulated suspension force waveform along y-axis 53
46 **Figure 46**: Step Change and Motor Current Dynamics – **(a)** x-axis rotor position, **(b)** y-axis rotor position, **(c)** Suspension current waveform in d-axis, **(d)** Suspension current waveform in q-axis, **(e)** Simulated suspension force waveform along x-axis, **(f)** Simulated suspension force waveform along y-axis 54
47 **Figure 47**: Step Input and Output Disturbances Dynamics – **(a)** x-axis rotor position, **(b)** y-axis rotor position, **(c)** Suspension current waveform in d-axis, **(d)** Suspension current waveform in q-axis, **(e)** Simulated suspension force waveform along x-axis, **(f)** Simulated suspension force waveform along y-axis 55

List of Tables

1 Nominal Values in Rotor Reference Frame 9
2 Pros and Cons of Controller and State-Command 56
3 Pros and Cons of Controller, Estimator and Integral 56

1 Introduction

1.1 Background

During the course of the last few years, investigations and research regarding electric drives and their control have stepped up many a fold. This is due to the fact that, apart from the machine, many power electronic systems are involved with them. Hence, there is a sudden need to reduce, as much as possible, such power electronic components. It will get the working system rid of superfluous complexity and simultaneously cut down on the carbon footprint in the world.

When the system in itself bears less complexity, modelling becomes easier. Hence, simpler yet efficacious control techniques can be implemented on such modelled systems for research and investigative purposes. Simulations become easier and practical tests can be conducted without too much hassle. In the last few years, an innovative technology, called bearingless systems, have gained popularity because of their simple design and lesser number of associated power electronic components.

Bearingless drives, also called direct or gearless drives, for high-speed applications replace the low-speed drives with mechanical step-up gears[1]. Bearingless systems have the advantage of maintenance-free operation, high durability and high speed without any mechanical friction, vibrations or lubrication, which are generally necessary for mechanical bearings. These attributes make the bearingless motors attractive for precision and in-vacuum applications[2][3]. In order to ensure stable operation of such bearingless drives, maintaining the magnetically-levitated rotor in the central position and using active control and feedback is essential. Oscillations in the rotor position will lead to instability and losses.

1.2 Previous Works

Control of Active Magnetic Bearings (AMB) systems has been designed and implemented through Field Programmable Gate Array (FPGA) based Linear Quadratic control (LQC)[4]. Efficiency of 5 kW and 50 kW prototypes with 4-pole motor windings and 2-pole suspension windings have also been conducted[5]. Furthermore, design and computer analysis of a 100 kW bearingless motor have been done following some already available but previously univestigated novel design methods[6][7][8][9]. The research works form the basis and motivation for this research work. Here, model-based approach has been considered for bearingless motor control, and the feasibility has been tested.

1.3 Objectives of Thesis

This thesis aims to meet the following targets:

(1) Develop a Discrete Linear-Quadratic Controller for a bearingless system

(2) Develop a Kalman Estimator for the same system in order to counter any unmeasured states and filter noisy output

(3) Achieve the stability of the magnetically-levitated rotor right at the center position of a real bearingless machine

(4) Test the control strategy with five different combinations of controller, estimator, integrator and state-command path and then, compare them with each other

(5) Investigate the motor and levitation control coupling and disturbances.

The Discrete Linear-Quadratic controller (DLQC) employs minimization of a cost function. The controller gains for the system are computed by assigning values to the weight matrices. The controller, in itself, is based on the steady-state solution of the levitation of the rotor. A discrete controller, with an appropriate sampling time, is used so that the delay in the communication between the various subsystems can also be taken into account.

Kalman Estimator (KE) is deployed in order to account for the unmeasured states, if any, of the system. The system is observable (evidences are provided later on in the document), and hence the estimator is fitted in order to supply the correct values of the states to the controller. Sometimes it may so happen that due to process or output disturbances, some erroneous results are recorded. In such cases, appropriate control signals are not generated when negative loop is used in the system. The system might then lose stability. Hence, the Kalman estimator is used for the system.

The integrator is used alongwith the controller and estimator in order to bring the steady-state errors down to a minimum. It has already been mentioned before that the gains for the controller are itself based on the steady-state solution. State-command path is also included while forming the closed-loop system. These control strategies are then compared and comments on the better ones are provided in the end.

1.4 Outline of Thesis

This thesis is segregated into seven chapters. These seven chapters are further broken down into several subsections, depending upon the relative importance of each with respect to the aim of this thesis. Comparisons amongst different control strategies chosen for the investigation of the stability of the system are sufficiently explained. The entire work is organized as follows:

Chapter 1 provides the background, previous works, objectives and outline of the thesis.

Chapter 2 briefly throws light on the previous applications of bearingless motors. Later, it explains the modelling of the bearingless motor for this research work and provides the state-space representation of the suspension forces acting on the leviatated rotor.

Chapter 3 shows the control strategies involving controller and controller and state-command path considered for the system. The overall control structures for the system involving such control strategies are presented right at the beginning of each subchapter for better visualization of the control structures. The step responses and frequency responses for the system with these control strategies are then shown. Comparisons between the two strategies by showing how the outputs and the control signals change with respect to time due to step reference, step input and output disturbances are drawn towards the end.

Chapter 4 show the control strategies involving controller and estimator and controller, estimator and state-command path considered for the system. Just like in *Chapter 3*, the control structures with these control strategies are provided right at the beginning. The step and frequency responses are shown followed by comparisons between the two control strategies considered for the system in this chapter.

Chapter 5 deals with control strategy which includes controller, estimator and integrator. The control structure is present right at the beginning. Again the step and frequency responses are shown. Output and control signal responses are presented and discussed in detail.

Chapter 6 presents the comparisons of the stable control strategies amongst the ones developed for the system. It discusses the pros and cons of those control strategies and provides comments on the ultimate selection between them.

Chapter 7 includes the conclusion which briefly describes the problem, methods used for solving the problem, the results obtained and provides advices for possible future research work on such an interesting and emerging topic.

2 Bearingless Systems

2.1 Applications

Several applications of motors with bearingless technology have been cited in literature before. Some of them are presented here for clearer comprehension. Industrial canned pump applications can be best achieved with controlld consequent pole permanent magnet (PM) motors because of wide magnetic air-gaps with respect to their rotor radius[10][11][12][13]. Reluctance motors with bearingless technology have applications in high temperature or intense temperature variation operations due to their advantages like fail safe, robustness and low cost[10][14][15][16]. Bearingless induction motors have the advantage that they can be levitated with lesser voltage-ampere requirements[10][17]. They have additional windings in the stator, but that doesn't stop them from being used in pumps or compressors. One instance of such applications was already proposed in 2002[18]. Over here, centrifugal pumps were designed without bearings or seals. Such centrifugal pumps were later used in medical applications, where flow rates of upto 18 litres could be easily achieved. Axial-type self-bearing motors were first developed in 2005 in order to be used as an artificial blood pump[19][20]. Such a pump was designed in order to pump blood during cardiopulmonary by-pass. 300 W permanent magnet synchronous motor (PMSM) was designed in 2012 for bioreactor mixing[21]. Low-shear agitation is a compulsory requirement in such bioreactors. Bearingless motors with 2500 W power and 50 Nm torque production capability were designed in 2012 for use in pharmaceutical mixing applications[22]. Pharmaceutical industries generally use stirred vessels. However, leakages, lubricants and mechanical wear may bring about contamination of the process fluid. Hence, in order to curb such drawbacks, magnetically levitated motors were especially designed to achieve a sealed, encapsulated tank design, so that contamination could be stopped. Bearingless motors have also found applications in wastewater treatment plants[23]. During the motor design process, certain parameters were considered. Efficiency, low capital cost, zero maintenance cost, remote monitoring capabilities are some of the criteria which were kept in mind during the motor design process.

2.2 Modelling of Bearingless Motor

A good, precise model is generally created around the dynamics of the system so that the steady-state characteristics of the entire system can be accurately investigated. For this thesis' investigation purposes, those dynamics are then converted into state-space models. The procedure for the modelling and choice of the states for conversion to state-space models are presented below.

2.3 Flux Linkages and Winding Currents

A control system for bearingless motors include levitation control subsystem and motion control subsystem. For this thesis, levitation control strategies have been

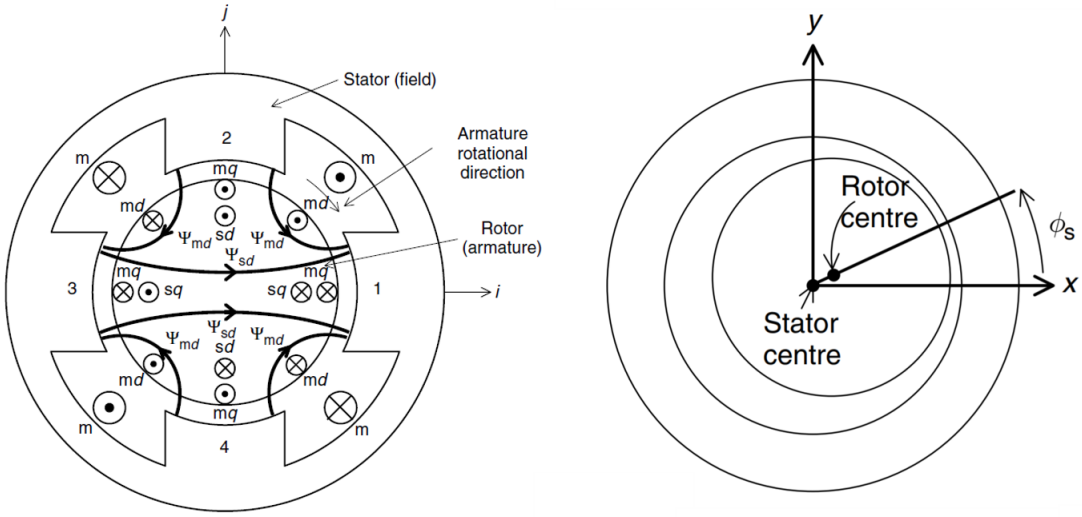

Figure 1: Winding Arrangements in Rotor Co-Ordinates (left) and Relative Positions of Stator and Rotor during an operation(right)[9]

investigated. The dynamics of such a system involve the flux linkages and winding coil currents. The relation between flux linkages and winding coil currents is pretty essential here because that relation will form the starting point of the conversion of the dynamics into state-space models for the system. Figure 1 shows the winding arrangement of the bearingless motor, in rotational co-ordinates and the relative positions of stator and rotor during any operation[9]. The co-ordinates 'i' and 'j' in the figure on the left are equivalent to the co-ordinates 'x' and 'y' in the figure on the right.

There are actually two sets of 2-phase windings on the stator − one set is for motor operation, called the motor windings, and the other set is for creating the necessary magnetic field in order to levitate the rotor, called the suspension windings, during motor operations. The suspension windings carry the suffix 's' and the motor windings carry the suffix 'm'. The currents are fed into both the windings from the *direct* axis (often abbreviated as d-axis) and *quadrature* axis (often referred to as q-axis). Hence, both of these windings carry additional suffixes like 'd' and 'q'.

The rotor center has to be aligned with the stator center during the motor operations and that is the goal for this thesis. The stator center can be considered to be at Cartesian co-ordinates [0,0] and this is exactly where the rotor center should be when it is kept suspended by the currents in the suspension windings during motor operations. The suspension windings are so arranged that the suspension forces are always produced along the x- and y-axes. A state-of-the-art control strategy has to be designed so that the cross-coupling of the magneto-motive forces (MMFs), induced by the motor windings, with the suspesion forces have minimal effect on the levitation of the rotor. Since fluxes are also produced due to the electromagnetic action here, the flux linkages from both the suspension and motor windings have direct relations with the suspension and motor windings' currents.

The relationship between the flux linkages and winding currents can be expressed in the form of equations as presented below[9]

$$\begin{bmatrix} \Psi_{md} \\ \Psi_{mq} \\ \Psi_{sd} \\ \Psi_{sq} \end{bmatrix} = \begin{bmatrix} L_d & 0 & M_d^{'}x & -M_d^{'}y \\ 0 & L_q & M_q^{'}y & M_q^{'}x \\ M_d^{'}x & M_q^{'}y & L_s & 0 \\ -M_d^{'}y & M_q^{'}x & 0 & L_s \end{bmatrix} \begin{bmatrix} i_{md} \\ i_{mq} \\ i_{sd} \\ i_{sq} \end{bmatrix} + \begin{bmatrix} \lambda_m \\ 0 \\ \lambda_m^{'}x \\ -\lambda_m^{'}y \end{bmatrix} \tag{1}$$

where,
Ψ_{md} = flux linkage of the motor in $d-$axis winding,
Ψ_{mq} = flux linkage of the motor in $q-$axis winding,
Ψ_{sd} = flux linkage of the suspension in $d-$axis winding,
Ψ_{sq} = flux linkage of the suspension in $q-$axis winding,
L_d = $d-$axis self-inductance,
L_q = $q-$axis self-inductance,
$M_d^{'}$ = suspension force constant in $d-$axis,
$M_q^{'}$ = suspension force constant in $q-$axis,
i_{md} = $d-$axis motor winding coil current,
i_{mq} = $q-$axis motor winding coil current,
i_{sd} = $d-$axis suspension winding coil current,
i_{sq} = $q-$axis suspension winding coil current,
λ_m = flux linkage caused by stator magnetic field,
$\lambda_m^{'}$ = current stiffness in active magnetic bearings,
x = displacement in the x-axis,
y = displacement in the y-axis

The stored magnetic co-energy ($W_m^{'}$) can be derived by using the above flux linkage-winding current relationship. If there is no saturation, then the magnetic co-energy ($W_m^{'}$) is equal to the stored magnetic energy (W_m)[9].

$$W_m^{'} = W_m = \frac{1}{2}\begin{bmatrix} i_{md} & i_{mq} & i_{sd} & i_{sq} \end{bmatrix} \begin{bmatrix} \Psi_{md} \\ \Psi_{mq} \\ \Psi_{sd} \\ \Psi_{sq} \end{bmatrix} \tag{2}$$

Substituting Eq (1) into Eq (2) eventually yields

$$\begin{aligned} W_m = {} & \frac{1}{2}(L_d i_{md}^2 + L_q i_{mq}^2 + L_s i_{sd}^2 + L_s i_{mq}^2) \\ & + (M_d^{'}x i_{md} i_{sd} - M_d^{'}y i_{md} i_{sq} + M_q^{'}y i_{mq} i_{sd} + M_q^{'}x i_{mq} i_{sq}) \\ & + \frac{1}{2}(i_{md}\lambda_m + \Psi_m^{'}x i_{sd} - \Psi_m^{'}y i_{sq}) \end{aligned} \tag{3}$$

2.4 Suspension Forces

Although Eq (3) is based on non-holonomic systems with only rotational movement, the derived suspension forces are valid because these forces are obtained from partial derivatives with respect to radial displacements[9].

The suspension forces are

$$F_x = \frac{\partial W_{\mathrm{m}}}{\partial x} = \left(\frac{1}{2}\lambda_{\mathrm{m}}^{'} + M_d^{'} i_{\mathrm{m}d}\right) i_{\mathrm{s}d} + (M_q^{'} i_{\mathrm{m}q}) i_{\mathrm{s}q} \tag{4}$$

$$F_y = \frac{\partial W_{\mathrm{m}}}{\partial y} = (M_q^{'} i_{\mathrm{m}q}) i_{\mathrm{s}d} + \left(-\frac{1}{2}\lambda_{\mathrm{m}}^{'} - M_d^{'} i_{\mathrm{m}d}\right) i_{\mathrm{s}q} \tag{5}$$

Eq (4) and Eq (5) can be arranged in simple matrix form as

$$\begin{bmatrix} F_x \\ \\ F_y \end{bmatrix} = \begin{bmatrix} \frac{1}{2}\lambda_{\mathrm{m}}^{'} + M_d^{'} i_{\mathrm{m}d} & M_q^{'} i_{\mathrm{m}q} \\ \\ M_q^{'} i_{\mathrm{m}q} & -\frac{1}{2}\lambda_{\mathrm{m}}^{'} - M_d^{'} i_{\mathrm{m}d} \end{bmatrix} \begin{bmatrix} i_{\mathrm{s}d} \\ \\ i_{\mathrm{s}q} \end{bmatrix} \tag{6}$$

Here, the radial positions are being controlled and it is assumed that motor current in d-axis ($i_{\mathrm{m}d}$) ≈ 0 during the entire operation of the PM motor. In that case, Eq (6) takes the following form

$$\begin{bmatrix} F_x \\ \\ F_y \end{bmatrix} = \begin{bmatrix} 0.5\lambda_{\mathrm{m}}^{'} & M_q^{'} i_{\mathrm{m}q} \\ \\ M_q^{'} i_{\mathrm{m}q} & -0.5\lambda_{\mathrm{m}}^{'} \end{bmatrix} \begin{bmatrix} i_{\mathrm{s}d} \\ \\ i_{\mathrm{s}q} \end{bmatrix} \tag{7}$$

In addition to the suspension currents, the radial forces also have dependency on the position stiffnesses of the motor and gravitational force. Hence, when those two are added with the suspension forces due to eccentricity, Eq (7) can be re-written as

$$\begin{bmatrix} F_x \\ \\ F_y \end{bmatrix} = \begin{bmatrix} (k_{x1} + k_{x2} i_{\mathrm{m}q}) x \\ \\ (k_{x1} + k_{x2} i_{\mathrm{m}q}) y \end{bmatrix} + \begin{bmatrix} 0.5\lambda_{\mathrm{m}}^{'} & M_q^{'} i_{\mathrm{m}q} \\ \\ M_q^{'} i_{\mathrm{m}q} & -0.5\lambda_{\mathrm{m}}^{'} \end{bmatrix} \begin{bmatrix} i_{\mathrm{s}d} \\ \\ i_{\mathrm{s}q} \end{bmatrix} + \begin{bmatrix} 0 \\ \\ -mg_a \end{bmatrix} \tag{8}$$

where, k_{x1} and k_{x2} are position stiffnesses respectively, m is the point mass of the rotor and g_a is the acceleration due to gravity. The values for k_{x1} and k_{x2} are obtained through FEM analyses[6]. During initial lift-up, the non-diagonal terms are zero as $i_{\mathrm{m}q}$ is assumed to be zero.

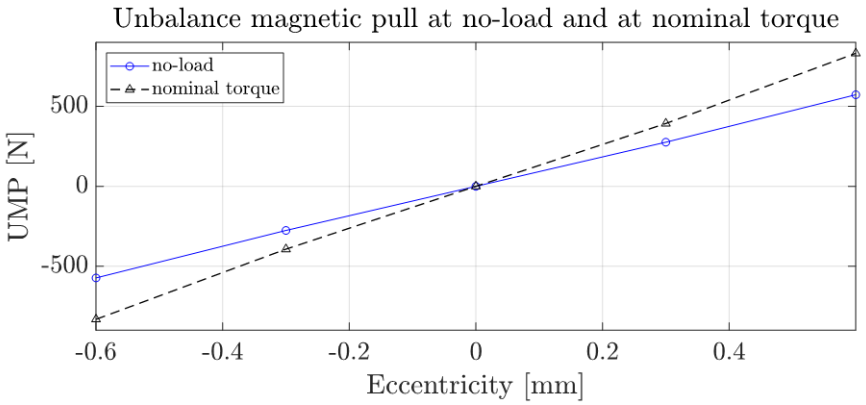

Figure 2: Unbalance magnetic pull at no-load and at nominal torque[6]

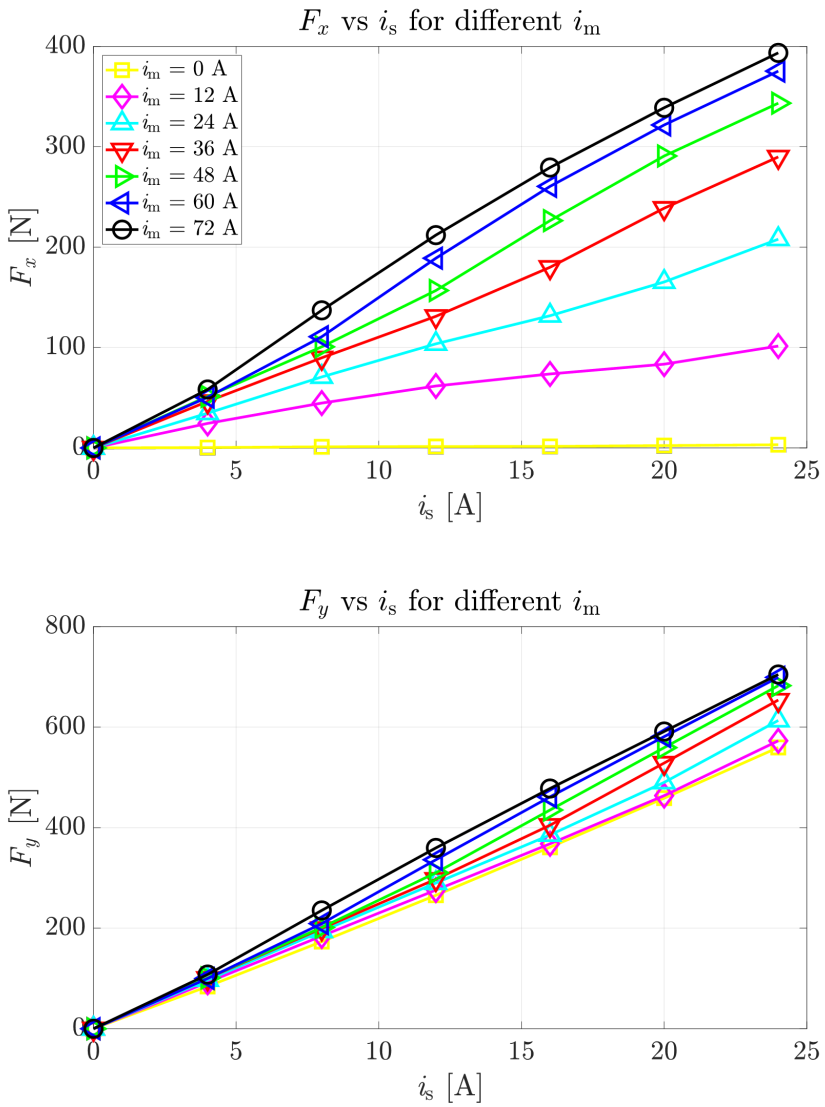

Figure 3: Forces in x- and y-directions for different i_s and i_m values

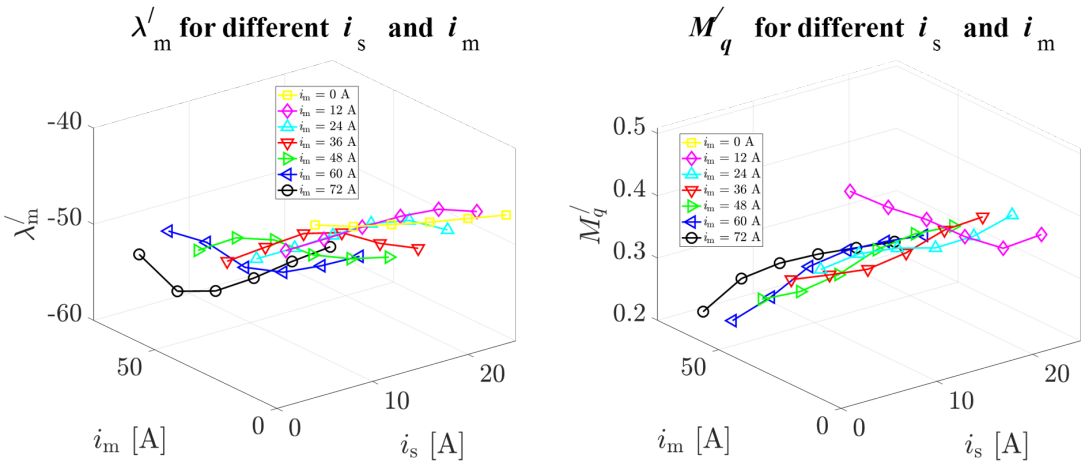

Figure 4: $\lambda_{\mathrm{m}}^{'}$ and $M_q^{'}$ for different i_{s} and i_{m} values

Table 1 – Nominal Values in Rotor Reference Frame

Quantities	Nominal Values	Ranges
i_{mq}^{rms}	42.43 (A)	-50.91 (A) $\leqslant i_{\mathrm{mq}}^{rms} \leqslant 50.91$ (A)
i_{sd}^{rms}	8.49 (A)	-16.97 (A) $\leqslant i_{\mathrm{sd}}^{rms} \leqslant 16.97$ (A)
i_{sq}^{rms}	8.49 (A)	-16.97 (A) $\leqslant i_{\mathrm{sq}}^{rms} \leqslant 16.97$ (A)
$\lambda_{\mathrm{m}}^{'}$	-56.85 (NA^{-1})	-59.95 (NA^{-1}) $\leqslant \lambda_{\mathrm{m}}^{'} \leqslant -50.00$ (NA^{-1})
$M_q^{'}$	0.26 (NA^{-2})	0.20 (NA^{-2}) $\leqslant M_q^{'} \leqslant 0.30$ (NA^{-2})
k_{x1}	954450 (Nm^{-1})	Not Applicable
k_{x2}	8480.6 (NA^{-1}m^{-1})	Not Applicable
m	8 (kg)	Not Applicable
g_a	9.81 (ms^{-2})	Not Applicable
a_g	0.9 (mm)	Not Applicable

Figure 2 presents the unbalance magnetic pull forces of single motor unit at no-load and nominal torque conditions. The magnetic pull forces are obtained from FEM simulations[6]. The permanent magnets in rotor generate radial force when the rotor is displaced from central position[9].

Figure 3 shows the force amplitudes in x- and y-directions with respect to suspension-force currents for several different motor current values. The forces are also obtained from FEM simulations[6].

Figure 4 describes the relationship of $\lambda_{\mathrm{m}}^{'}$ and $M_q^{'}$ for increasing values of both the motor current and suspension-force current. The values for $\lambda_{\mathrm{m}}^{'}$ and $M_q^{'}$ are obtained by utilizing the previous equations.

It can be observed from Figure 4 that, $\lambda_{\mathrm{m}}^{'}$ and $M_q^{'}$ remain almost constant around $i_{\mathrm{s}} = 12$ A. Hence, median of all the values of $\lambda_{\mathrm{m}}^{'}$ and $M_q^{'}$ are calculated and those calculated values are chosen to be the ones for nominal operation of the motor. The nominal i_{m} was finalized to be 60 A, based on the values of $\lambda_{\mathrm{m}}^{'}$ and $M_q^{'}$. All these values, which are later used for obtaining the controller and estimator gain matrices, in rotor reference frame are presented in Table 1.

2.5 State-Space Models

2.5.1 Model Structure

In order to form the state-space equations from Eq (8), the positions and velocities in x- and y-directions are considered to be the states. Hence, the state vector is taken to be

$$\mathbf{x} = \begin{bmatrix} \dot{x} \\ x \\ \dot{y} \\ y \end{bmatrix}$$

2.5.2 State-Space Matrices

Expressing $F = ma_{cc}$, where m is the point-mass of the rotor and a_{cc} ($= \ddot{x}$ or $\ddot{y}$) is the acceleration, the state-space equations are given by Eq (9). The $\mathbf{x}$ matrix, in Eq. (9), constitutes the states of the system and $\mathbf{u}$ contains all the inputs. The gravitational force is considered to be a disturbance for the system and hence not considered for forming the state-space equations. It was separately added as a disturbance later during further investigations.

$$\underbrace{\begin{bmatrix} \ddot{x} \\ \dot{x} \\ \ddot{y} \\ \dot{y} \end{bmatrix}}_{\dot{\mathbf{x}}} = \underbrace{\begin{bmatrix} 0 & \left(\frac{k_{x1} + k_{x2} i_{\mathrm{mq}}}{m}\right) & 0 & 0 \\ 1 & 0 & 0 & 0 \\ 0 & 0 & 0 & \left(\frac{k_{x1} + k_{x2} i_{\mathrm{mq}}}{m}\right) \\ 0 & 0 & 1 & 0 \end{bmatrix}}_{\mathbf{A}} \underbrace{\begin{bmatrix} \dot{x} \\ x \\ \dot{y} \\ y \end{bmatrix}}_{\mathbf{x}} + \underbrace{\begin{bmatrix} \left(\frac{0.5\lambda_{\mathrm{m}}^{'}}{m}\right) & \left(\frac{M_q^{'} i_{\mathrm{mq}}}{m}\right) \\ 0 & 0 \\ \left(\frac{M_q^{'} i_{\mathrm{mq}}}{m}\right) & \left(\frac{-0.5\lambda_{\mathrm{m}}^{'}}{m}\right) \\ 0 & 0 \end{bmatrix}}_{\mathbf{B}} \underbrace{\begin{bmatrix} i_{\mathrm{sd}} \\ i_{\mathrm{sq}} \end{bmatrix}}_{\mathbf{u}} + \tag{9}$$

$$\dot{\mathbf{x}} = \underbrace{\begin{bmatrix} 0 & 164.281 & 0 & 0 \\ 1 & 0 & 0 & 0 \\ 0 & 0 & 0 & 164.281 \\ 0 & 0 & 0 & 1 \end{bmatrix}}_{\mathbf{A}} \mathbf{x} + \underbrace{\begin{bmatrix} -0.004 & 0.001 \\ 0 & 0 \\ 0.001 & 0.004 \\ 0 & 0 \end{bmatrix}}_{\mathbf{B}} \mathbf{u} \tag{10}$$

$$\mathbf{y}_{\text{out}} = \begin{bmatrix} x \\ y \end{bmatrix} = \underbrace{\begin{bmatrix} 0 & 1 & 0 & 0 \\ 0 & 0 & 0 & 1 \end{bmatrix}}_{\mathbf{C}} \mathbf{x} + \underbrace{\begin{bmatrix} 0 & 0 \\ 0 & 0 \end{bmatrix}}_{\mathbf{D}} \mathbf{u} \tag{11}$$

For the ease of the radial position control, the coupling due to MMF generated by i_{mq} needs to be kept at a minimum, so that steady-state performances of the levitated rotor can be free from any unwanted system disturbances. According to the control strategy, there must also be minimal diagonal effect. Diagonal effect can be defined here as the change in y-axis rotor position due to changes in d-axis suspension current. The effect is also valid for relationship between x-axis rotor position and q-axis suspension current. This diagonal effect should not take place in the controlled system, since maintaining the levitation could become a tiresome affair. Eq (9) and Eq (10) present the state-space equations of the system, before and after replacing the parameters with their nominal values from Table 1. **A**, **B**, **C** and **D** are the state-space matrices. The outputs for the system are the radial positions of the rotor. The state-space equation for the output ($\mathbf{y}_{\text{out}}$) is shown in Eq (11).

2.5.3 Per-Unit Matrices

In control and power system analysis, it is a common practice to use per-unit quantities for analyzing and communicating voltage, current, power, and impedance values. These per-unit quantities are normalized or scaled on a selected base, allowing engineers to simplify system calculations with multiple transformations.

In our case, per-unit quantities, in the form of matrices, are required for $\mathbf{x}$, $\mathbf{u}$, $\mathbf{y}_{\text{out}}$ and $\dot{\mathbf{x}}$ vectors. These matrices need to be transformed into their per-unit quantities and for that, $\mathbf{T}_{\text{x}}$, $\mathbf{T}_{\text{u}}$ and $\mathbf{T}_{\text{yout}}$ need to be defined here.

Definition of $\mathbf{T}_{\text{x}}$

Now, $\mathbf{x} = [\dot{x} \;\; x \;\; \dot{y} \;\; y]^{\text{T}}$ contains the velocity and the position values. Hence, in order to define a transformation matrix for such a matrix, the diagonal values for that transformation matrix need to be, in the respective order, the reciprocal of the maximum values of the velocities and positions in the respective axes. The maximum velocity is taken to be 100 m/s and the maximum allowable rotor displacement from

the central position is the air-gap (0.9 mm). Therefore, the transformation matrix $\mathbf{T}_{\mathrm{x}}$ will have the following form

$$\mathbf{T}_{\mathrm{x}} = \begin{bmatrix} \frac{1}{\dot{x}_{\max}} & 0 & 0 & 0 \\ 0 & \frac{1}{x_{\max}} & 0 & 0 \\ 0 & 0 & \frac{1}{\dot{y}_{\max}} & 0 \\ 0 & 0 & 0 & \frac{1}{y_{\max}} \end{bmatrix}$$

$$\text{or, } \mathbf{T}_{\mathrm{x}} = \begin{bmatrix} \frac{1}{1000} & 0 & 0 & 0 \\ 0 & \frac{1}{0.9 \times 10^{-3}} & 0 & 0 \\ 0 & 0 & \frac{1}{1000} & 0 \\ 0 & 0 & 0 & \frac{1}{0.9 \times 10^{-3}} \end{bmatrix}$$

Definition of $\mathbf{T}_{\mathbf{u}}$

Now, $\mathbf{u}$ contains the suspension winding coil current values. Hence, the transformation matrix needs to contain, in respective order, the reciprocal of the maximum values of these currents (24 A). The transformation matrix also needs to be diagonal in order to get the per-unit values in the same order as the original $\mathbf{u}$ matrix.

$$\mathbf{T}_{\mathrm{u}} = \begin{bmatrix} \frac{1}{\dot{i}_{sd\max}} & 0 \\ 0 & \frac{1}{\dot{i}_{sq\max}} \end{bmatrix}$$

$$\text{or, } \mathbf{T}_{\mathrm{u}} = \begin{bmatrix} \frac{1}{24} & 0 \\ 0 & \frac{1}{24} \end{bmatrix}$$

Definition of $\mathbf{T}_{\mathbf{yout}}$

For the per-unit transformation of the $\mathbf{y}_{\mathrm{out}}$ matrix, only the maximum position values are sufficient. Hence, the transformation matrix will look like $\rightarrow$

$$\mathbf{T}_{\mathrm{yout}} = \begin{bmatrix} \frac{1}{x_{\max}} & 0 \\ 0 & \frac{1}{y_{\max}} \end{bmatrix}$$

$$\text{or, } \mathbf{T}_{\text{yout}} = \begin{bmatrix} \dfrac{1}{0.9 \times 10^{-3}} & 0 \\ 0 & \dfrac{1}{0.9 \times 10^{-3}} \end{bmatrix}$$

Definition of $\mathbf{x_{pu}}$

The per-unit matrix ($\mathbf{x}_{\text{pu}}$), containing all the states, can be derived by directly multiplying the $\mathbf{T}_{\text{x}}$ matrix with $\mathbf{x}$ matrix.

$$\begin{aligned} \mathbf{x}_{\text{pu}} &= \mathbf{T}_{\text{x}}\mathbf{x} \\ \text{or, } \mathbf{x} &= \mathbf{T}_{\text{x}}^{-1}\mathbf{x}_{\text{pu}} \end{aligned}$$

Definition of $\mathbf{u_{pu}}$

Similarly, in order to define $\mathbf{u}_{\text{pu}}$, $\mathbf{T}_{\text{u}}$ is multiplied with $\mathbf{u}$.

$$\begin{aligned} \mathbf{u}_{\text{pu}} &= \mathbf{T}_{\text{u}}\mathbf{u} \\ \text{or, } \mathbf{u} &= \mathbf{T}_{\text{u}}^{-1}\mathbf{u}_{\text{pu}} \end{aligned}$$

Definition of $\mathbf{y_{outpu}}$

$\mathbf{y}_{\text{outpu}}$ can be defined as

$$\begin{aligned} \mathbf{y}_{\text{outpu}} &= \mathbf{T}_{\text{yout}}\mathbf{y}_{\text{out}} \\ \text{or, } \mathbf{y}_{\text{out}} &= \mathbf{T}_{\text{yout}}^{-1}\mathbf{y}_{\text{outpu}} \end{aligned}$$

Definition of $\dot{\mathbf{x}}_{\mathbf{pu}}$

Similarly, $\dot{\mathbf{x}}_{\text{pu}}$ can be defined as

$$\begin{aligned} \dot{\mathbf{x}}_{\text{pu}} &= \mathbf{T}_{\text{x}}\dot{\mathbf{x}} \\ \text{or, } \dot{\mathbf{x}} &= \mathbf{T}_{\text{x}}^{-1}\dot{\mathbf{x}}_{\text{pu}} \end{aligned}$$

Definition of $\mathbf{A_{pu}}$ and $\mathbf{B_{pu}}$

The transformed matrices $\mathbf{A}_{\text{pu}}$ and $\mathbf{B}_{\text{pu}}$ become

$$\begin{aligned} \dot{\mathbf{x}} &= \mathbf{A}\mathbf{x} + \mathbf{B}\mathbf{u} \\ \text{or, } \mathbf{T}_{\text{x}}^{-1}\dot{\mathbf{x}}_{\text{pu}} &= \mathbf{A}\mathbf{T}_{\text{x}}^{-1}\mathbf{x}_{\text{pu}} + \mathbf{B}\mathbf{T}_{\text{u}}^{-1}\mathbf{u}_{\text{pu}} \\ \text{or, } \dot{\mathbf{x}}_{\text{pu}} &= \underbrace{\mathbf{T}_{\text{x}}\mathbf{A}\mathbf{T}_{\text{x}}^{-1}}_{\mathbf{A}_{\text{pu}}}\mathbf{x}_{\text{pu}} + \underbrace{\mathbf{T}_{\text{x}}\mathbf{B}\mathbf{T}_{\text{u}}^{-1}}_{\mathbf{B}_{\text{pu}}}\mathbf{u}_{\text{pu}} \end{aligned}$$

$$\text{or, } \dot{\mathbf{x}}_{\text{pu}} = \underbrace{\begin{bmatrix} 0 & 0 & 0 & 0 \\ 1.11 \times 10^6 & 0 & 0 & 0 \\ 0 & 0 & 0 & 0 \\ 0 & 0 & 1.11 \times 10^6 & 0 \end{bmatrix}}_{\mathbf{A}_{\text{pu}}} \mathbf{x}_{\text{pu}} + \underbrace{\begin{bmatrix} -0.84 \times 10^{-4} & 0.32 \times 10^{-4} \\ 0 & 0 \\ 0.32 \times 10^{-4} & 0.84 \times 10^{-4} \\ 0 & 0 \end{bmatrix}}_{\mathbf{B}_{\text{pu}}} \mathbf{u}_{\text{pu}} \tag{12}$$

Definition of $\mathbf{C_{pu}}$ and $\mathbf{D_{pu}}$

The transformed matrices $\mathbf{C}_{\text{pu}}$ and $\mathbf{D}_{\text{pu}}$ become

$$\begin{aligned} \mathbf{y}_{\text{out}} &= \mathbf{Cx} + \mathbf{Du} \\ \text{or, } \mathbf{T}_{\text{yout}}^{-1}\mathbf{y}_{\text{outpu}} &= \mathbf{C}\mathbf{T}_{\text{x}}^{-1}\mathbf{x}_{\text{pu}} + \mathbf{D}\mathbf{T}_{\text{u}}^{-1}\mathbf{u}_{\text{pu}} \\ \text{or, } \mathbf{y}_{\text{outpu}} &= \underbrace{\mathbf{T}_{\text{yout}}\mathbf{C}\mathbf{T}_{\text{x}}^{-1}}_{\mathbf{C}_{\text{pu}}}\mathbf{x}_{\text{pu}} + \underbrace{\mathbf{T}_{\text{yout}}\mathbf{D}\mathbf{T}_{\text{u}}^{-1}}_{\mathbf{D}_{\text{pu}}}\mathbf{u}_{\text{pu}} \\ \text{or, } \mathbf{y}_{\text{outpu}} &= \underbrace{\begin{bmatrix} 0 & 1 & 0 & 0 \\ 0 & 0 & 0 & 1 \end{bmatrix}}_{\mathbf{C}_{\text{pu}}}\mathbf{x}_{\text{pu}} + \underbrace{\begin{bmatrix} 0 & 0 \\ 0 & 0 \end{bmatrix}}_{\mathbf{D}_{\text{pu}}} \end{aligned} \tag{13}$$

2.5.4 Discretization

For discretization of a continuous process a sampling frequency is required. This sampling frequency (ω_s) must be, at least, greater than twice the natural frequency (ω_0) of the system itself; that is, in simple words $\omega_s > 2\omega_0$. The minimum sampling frequency, for which the inequality is valid, is known as *Nyquist angular frequency.*

There are also some criteria to choose the sampling frequency. The corresponding sampling period $\left(T_s = \dfrac{2\pi}{\omega_s} \right)$ needs to be:

- small enough, so that loss of information is negligible
- high enough, so that the system does not run out of computation power

A trade-off needs to be done between the two criteria mentioned above in order to get sufficient discrete-time information about the system. For the system, ω_s is taken to be approximately 1040π times as big as ω_0. The corresponding sampling time 100 μs is small enough for the information to be retained, and high enough for the system not to run out of memory. The state-space equations of the discretized

system is given by Eq (14). There are certainly no changes in the output equation after discretization of any process.

$$\mathbf{x}_{(k+1)\text{pu}} = \underbrace{\begin{bmatrix} 1.00 & 0 & 0 & 0 \\ 111.16 & 1.00 & 0 & 0 \\ 0 & 0 & 1.00 & 0.00 \\ 0 & 0 & 111.16 & 1.00 \end{bmatrix}}_{\mathbf{F}_{\text{pu}}} \mathbf{x}_{(k)\text{pu}} + \underbrace{\begin{bmatrix} -0.008 \times 10^{-6} & 0.003 \times 10^{-6} \\ -0.467 \times 10^{-6} & 0.180 \times 10^{-6} \\ 0.003 \times 10^{-6} & 0.008 \times 10^{-6} \\ 0.180 \times 10^{-6} & 0.467 \times 10^{-6} \end{bmatrix}}_{\mathbf{G}_{\text{pu}}} \mathbf{u}_{(k)\text{pu}} \tag{14}$$

where $\mathbf{F}_{\text{pu}}$ and $\mathbf{G}_{\text{pu}}$ are discrete equivalents of $\mathbf{A}_{\text{pu}}$ and $\mathbf{B}_{\text{pu}}$, respectively. These per-unit discrete matrices are used later in order to calculate controller gains, estimator gains, integrator gains and state-command path gains. However, the suffix 'pu' is not used later on just in order to keep everything neat and simple.

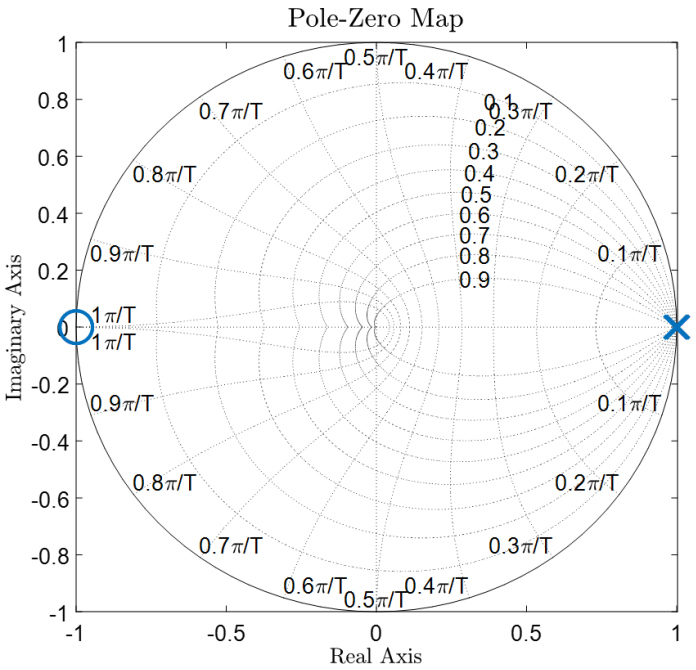

Figure 5: Pole-Zero Map of the Uncontrolled System

Figure 5 show the pole-zero map of the system. The relative gain array (**RGA**) of the entire per-unit discretized system was calculated out to be.

$$\mathbf{RGA} = \begin{bmatrix} 1 & 0 \\ 0 & 1 \end{bmatrix}$$

The diagonal values in the **RGA** are positive and small, indicating good decoupling and very low sensitivities to uncertainties in the system. The non-diagonal values are zero, indicating that coupling can be eliminated when control strategy is applied.

3 Linear Quadratic Controller

3.1 Controller Only

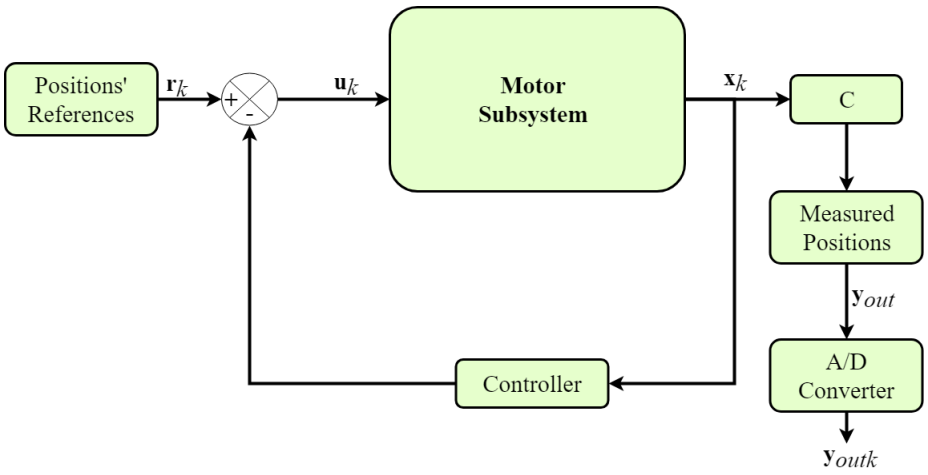

Figure 6: Controlled System's Structure with Controller Only

Figure 6 gives the structure for the controlled system when only the controller is present. The controllability matrix $\mathbf{W}_c = [\mathbf{G}\ \mathbf{FG}\ \mathbf{F}^2\mathbf{G}\ \ldots\ \mathbf{F}^{n-1}\mathbf{G}]$ (where n is the order of the system) does have a full rank for the system. Optimal control gains for the system are achieved by utilizing Discrete Linear Quadratic Regulator (DLQR) technique because addition of delays is relatively easier in case of DLQR compared to the same in case of Continuous-time Linear Quadratic Regulator (CLQR). Linear Quadratic controllers (LQC) give the advantage of being dynamic, since they generally depend on the state-space models and the weights put on them. The weight matrices, $\mathbf{Q}$ and $\mathbf{R}$, can be modified depending upon where the weights are wished to be put – on the states or on the input. Both the matrices will have to be symmetric and positive semi-definite.

In this type of a controller, an optimal solution has to be found which will minimize a cost function. Since the aim is to construct a discrete-time controller for the system the cost function in the discrete-time is

$$J = \sum_{k=1}^{\infty} (\mathbf{x}_k^{\mathrm{T}} \mathbf{Q} \mathbf{x}_k + \mathbf{u}_k^{\mathrm{T}} \mathbf{R} \mathbf{u}_k) \tag{15}$$

The controller gain matrix $\mathbf{K}$ is derived by

$$\mathbf{K} = (\mathbf{G}^{\mathrm{T}} \mathbf{S} \mathbf{G} + \mathbf{R})^{-1} (\mathbf{G}^{\mathrm{T}} \mathbf{S} \mathbf{F}) \tag{16}$$

where, $\mathbf{S}$ is the infinite horizon solution of the discrete-time Riccati equation

$$\mathbf{F}^{\mathrm{T}} \mathbf{S} \mathbf{F} - \mathbf{S} - (\mathbf{F}^{\mathrm{T}} \mathbf{S} \mathbf{G})(\mathbf{G}^{\mathrm{T}} \mathbf{S} \mathbf{G} + \mathbf{R}^{-1})(\mathbf{G}^{\mathrm{T}} \mathbf{S} \mathbf{F}) + \mathbf{Q} = 0 \tag{17}$$

The control law for the system can be given as

$$\mathbf{u}_k = -\mathbf{K}\mathbf{x}_k + \mathbf{r}_k \tag{18}$$

where,
$\mathbf{K}$ = Discrete controller matrix,
$\mathbf{x}_k$ = States in discrete time,
$\mathbf{r}_k$ = Reference signal in discrete time,

The selection of the weight matrices, $\mathbf{Q}$ and $\mathbf{R}$, is weakly connected to the optimal performance of the system on the whole. A certain amount of trial and error is required before satisfactory design results can be obtained. In the literature [24] and [25], it is suggested to take $\mathbf{Q} = \mathbf{H}^{\mathrm{T}}\overline{\mathbf{Q}}\mathbf{H}$ (where $\mathbf{H} = \mathbf{C}_{\mathrm{pu}}$) so that the states enter the cost via the important outputs. $\mathbf{Q}$ and $\mathbf{R}$ need to be selected with diagonal entries so that a fixed percentage change of each variable makes an equal contribution to the overall cost.

For the system, the maximum deviations of the outputs can be kept at 0.5 mm because the air-gap is 0.9 mm. So, the deviations are kept within almost half of air-gap, which is close to 0.5mm. The two outputs are considered to have equal contribution to the overall cost. By trial and error, a gain of 0.03 was added, for better damping. Therefore, the weight matrix $\mathbf{Q}$ have been carefully chosen as

$$\overline{\mathbf{Q}} = \begin{bmatrix} \dfrac{0.03}{(0.5\times 10^{-3})^2} & 0 \\ 0 & \dfrac{0.03}{(0.5\times 10^{-3})^2} \end{bmatrix} \tag{19}$$

$$\mathbf{H} = \begin{bmatrix} 0 & 1 & 0 & 0 \\ 0 & 0 & 0 & 1 \end{bmatrix} \tag{20}$$

$$\mathbf{Q} = \mathbf{H}^{\mathrm{T}}\overline{\mathbf{Q}}\mathbf{H} \tag{21}$$

The weight matrix $\mathbf{R}$, after adding the gain 0.03, is given as

$$\mathbf{R} = \begin{bmatrix} \dfrac{0.03}{(i_{\mathrm{sd}(max)})^2} & 0 \\ 0 & \dfrac{0.03}{(i_{\mathrm{sq}(max)})^2} \end{bmatrix} \tag{22}$$

Figure 7 shows the pole-zero map of the system after the implementation of only the controller. Comparing with Figure 5, it can be observed that the poles could be brought inside the unit circle, thus stabilizing the system. Figure 8 shows the step response of the same system. Figure 9 shows the reference-to-error sensitivity and Figure 10 shows the output-disturbance-to-output sensitivity when the system contains only the controller. The maximum allowable absolute value for both of them is 3, which approximates to 9.5 dB. The maximum values for both the sensitivities are well within that limit. It can be observed that, although the system is stable, given disturbances at the junction reference-to-system and system-to-output, the performance will tend to be sluggish and may not be upto the mark because of such a small gain.

Figure 11 shows the waveforms for controlled suspension currents in both the d- and q-axes in absence of q-axis motor current. Oscillations are observed in the q-axis suspension current as it has to initially fight against the additional force due to gravity and the controlled current itself cannot rise above 24 A or fall below -24 A as it is the mains supply current. The spikes appear in the waveforms when there are step changes in the rotor position. Figure 12 shows the responses of the rotor positions in x- and y-axes in absence of q-axis motor current. Responses to step changes in both x- and y-axes rotor positions are observed to be negligible, which go on to verify the sluggish nature or the conservatism of the controlled system.

Figure 13 shows the waveforms for controlled suspension currents in both the d- and q-axes in presence of q-axis motor current. It is observed from the figure that when q-axis motor current is started during the steady-state conditions of the rotor suspension dynamics, the controlled suspension currents lose their stability which also have an equally adverse effect on the hitherto nicely suspended rotor positions. Figure 14 shows the responses of the rotor positions in x- and y-axes in presence of q-axis motor current. The rotor positions in both x- and y-axes suffer due to the loss of stability in the controlled suspension currents when q-axis motor current is started.

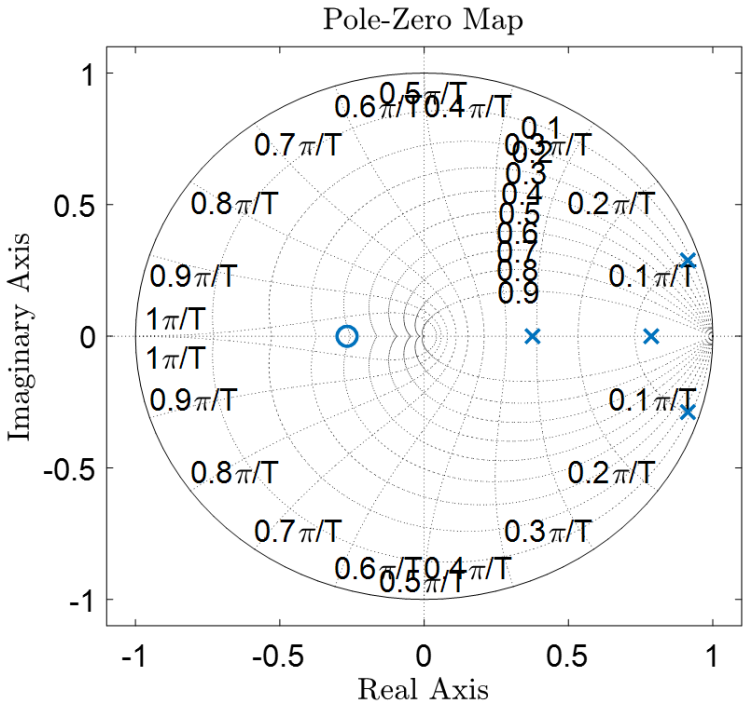

Figure 7: Pole-Zero Map of the System with Controller

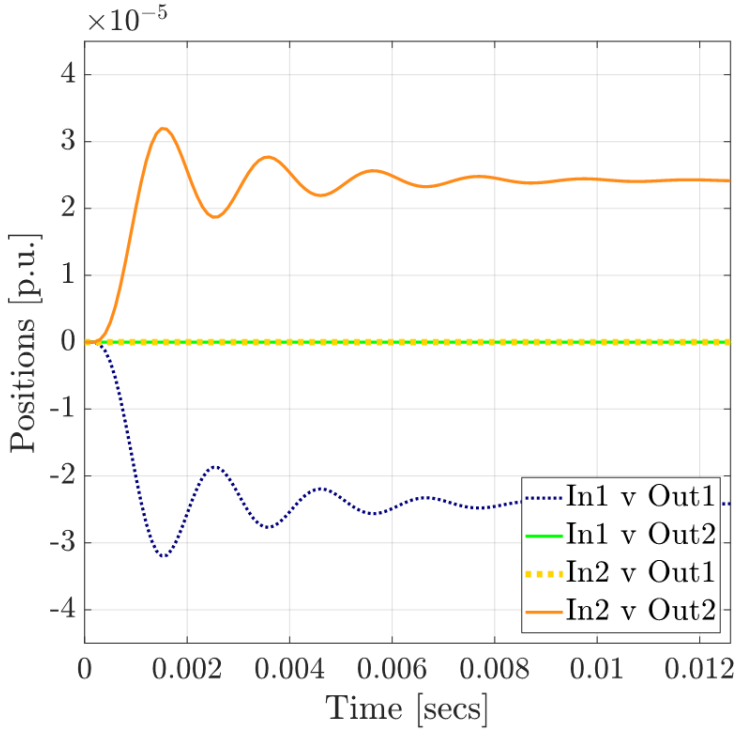

Figure 8: Step Response of the System with Controller

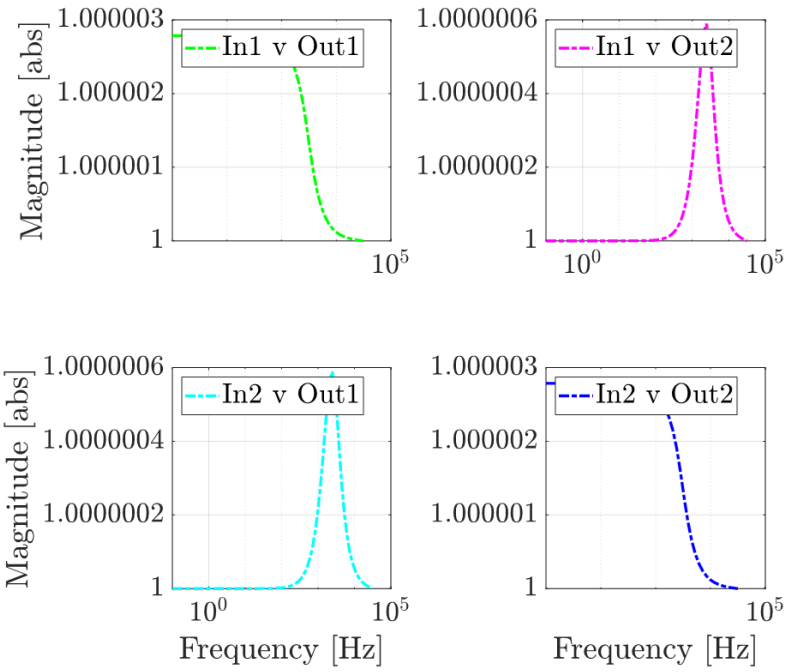

Figure 9: Reference-to-Error Sensitivity (System with controller)

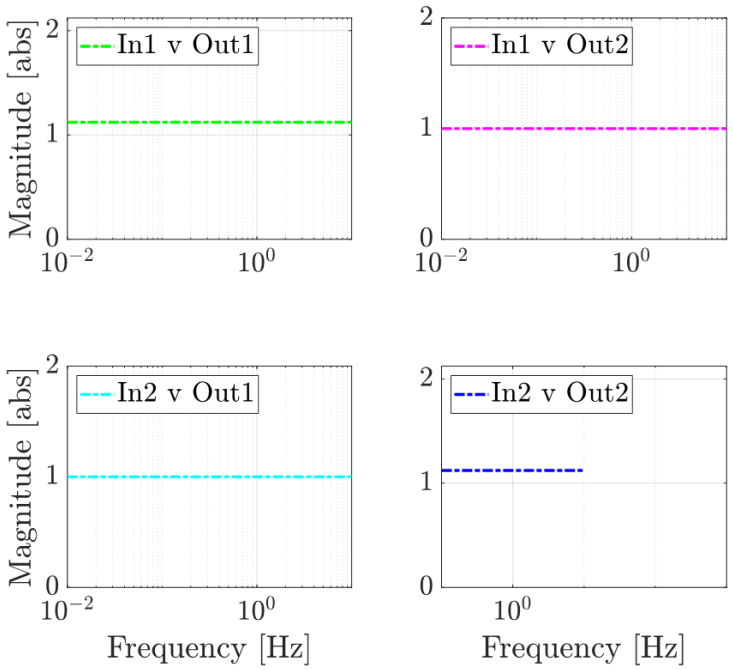

Figure 10: Output-disturbance-to-Output Sensitivity (System with Controller)

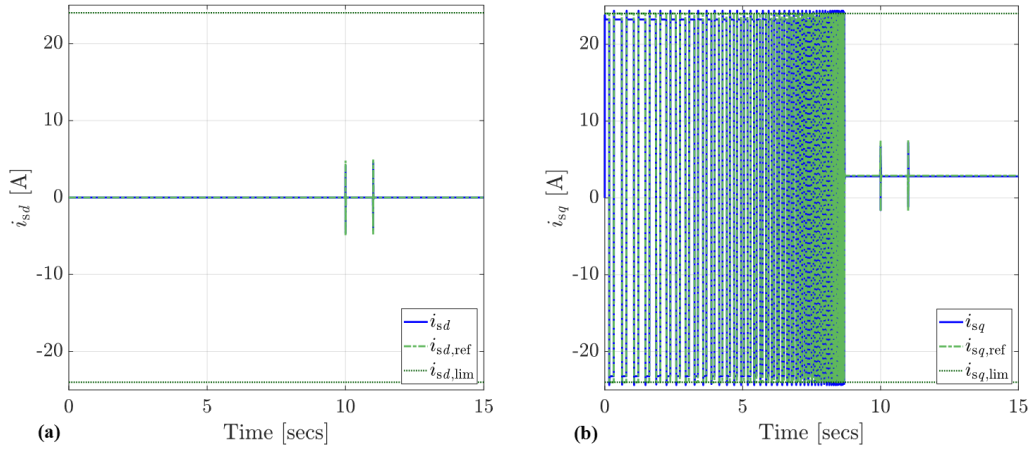

Figure 11: **(a)** Suspension current waveform in d-axis in absence of q-axis motor current, **(b)** Suspension current waveform in q-axis in absence of q-axis motor current

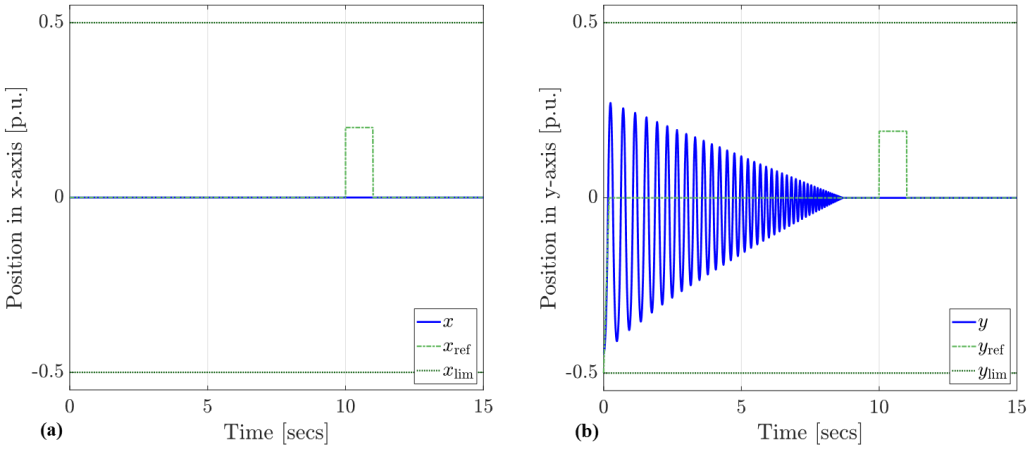

Figure 12: **(a)** x-axis rotor position responses in absence of q-axis motor current, **(b)** y-axis rotor position responses in absence of q-axis motor current

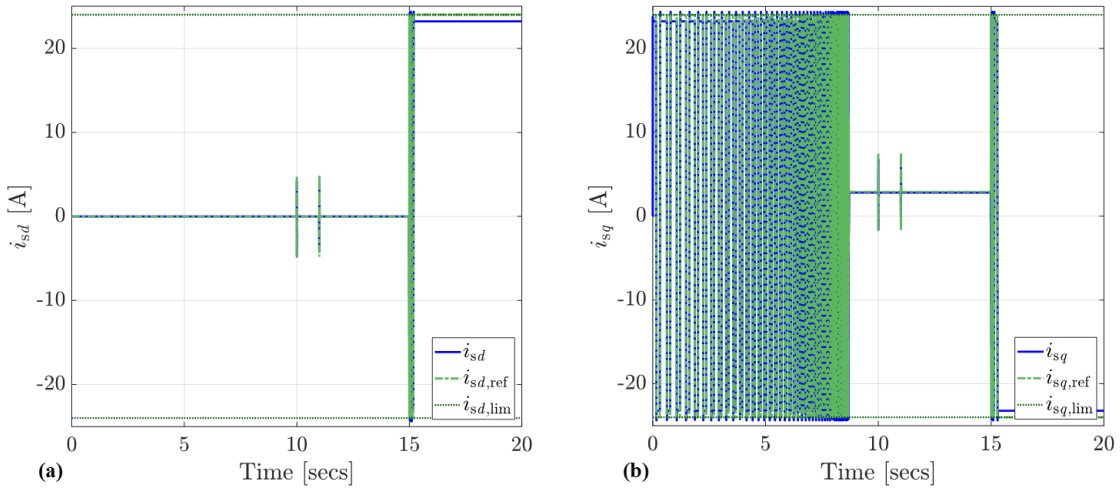

Figure 13: **(a)** Suspension current waveform in d-axis in presence of q-axis motor current, **(b)** Suspension current waveform in q-axis in presence of q-axis motor current

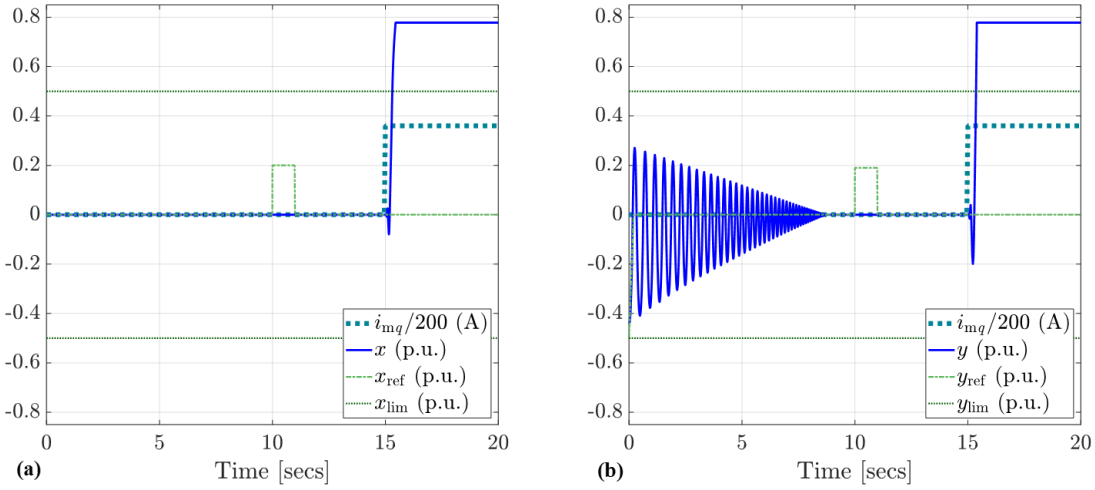

Figure 14: **(a)** x-axis rotor position responses in presence of q-axis motor current, **(b)** y-axis rotor position responses in presence of q-axis motor current

3.2 Controller with State-command Path

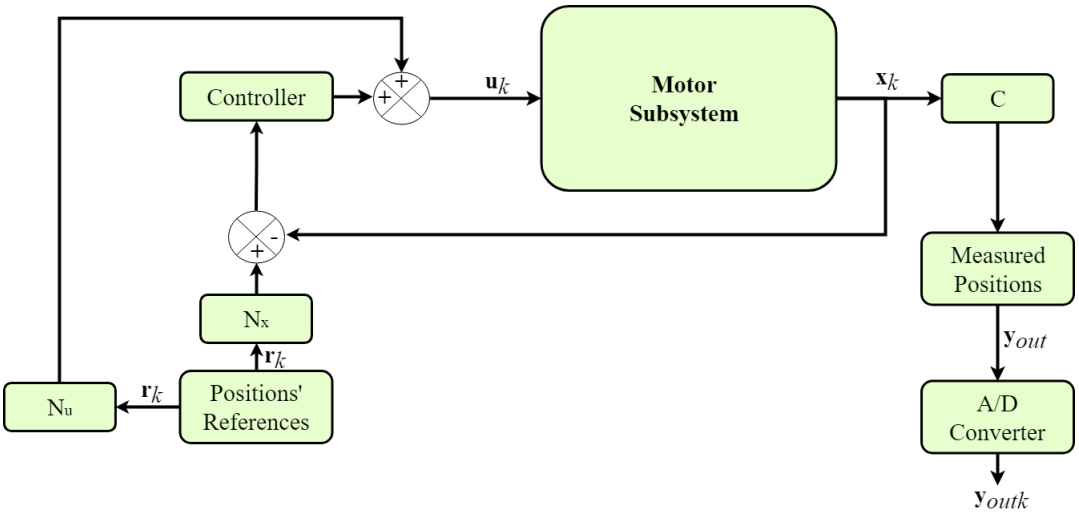

Figure 15: Controlled System's Structure with Controller and State-command path

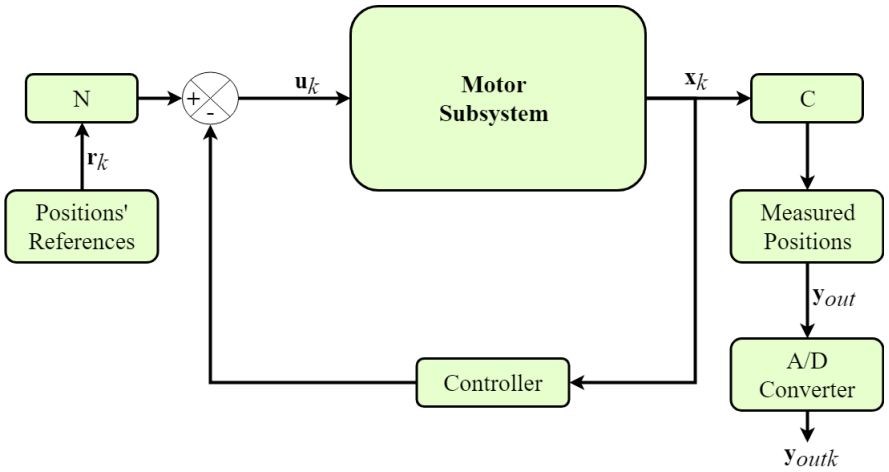

Figure 16: Controlled System's Structure with Controller and State-command path (Reduced Form)

In order to form the state-command path, a state-command matrix is required. The reason behind this state-command path is because the system is strictly proper and steady-state errors also exist, which can be determined from Figure 8. Hence, in order to minimize those steady-state errors, application of state-command path is being investigated here. The state-command matrices $\mathbf{N_x}$ and $\mathbf{N_u}$ can be given by[24]

$$\begin{bmatrix} \mathbf{N_x} \\ \mathbf{N_u} \end{bmatrix} = \begin{bmatrix} \mathbf{F}-\mathbf{I} & \mathbf{G} \\ \mathbf{C} & \mathbf{O} \end{bmatrix}^{-1} \begin{bmatrix} \mathbf{O} \\ \mathbf{I} \end{bmatrix} \tag{23}$$

The control law for this control strategy is

$$\begin{aligned} \mathbf{u}_k &= -\mathbf{K}\mathbf{x}_k + \mathbf{N}_{\mathrm{u}}\mathbf{r}_k + \mathbf{K}\mathbf{N}_{\mathrm{x}}\mathbf{r}_k \\ &= -\mathbf{K}\mathbf{x}_k + (\mathbf{N}_{\mathrm{u}} + \mathbf{K}\mathbf{N}_{\mathrm{x}})\mathbf{r}_k \\ \text{or, } \mathbf{u}_k &= -\mathbf{K}\mathbf{x}_k + \mathbf{N}\mathbf{r}_k \end{aligned} \tag{24}$$

where, $\mathbf{N} = \mathbf{N}_{\mathrm{u}} + \mathbf{K}\mathbf{N}_{\mathrm{x}}$. Figure 17 shows the pole-zero map of the system after the addition of state-command path with the controller. Comparing with Figure 7, it can be observed that some of the poles move closer to the boundary of the unit circle. Figure 18 shows the step response of the same system with the same control strategy. It can be observed that changes in input 1 affect only output 1 and similar is the case with input 2 and output 2, much like Figure 8. However, in Figure 18, the steady-state errors have been minimized, if not completely eliminated. Those steady-state errors were, however, present in Figure 8 which goes on to show that addition of state-command path does bring about some changes in the overall response of the system. However, small gains are observed once again in Figure 19 and Figure 20. Controlled currents' waveforms, positions' waveforms and forces' waveforms are hereafter recorded and shown.

Figure 21 shows the initial rotor lift-up dynamics of the controlled system with controller and state-command path. Figure 21(a) and Figure 21(b) show the d- and q-axes suspension current waveforms during the same stage. It is observed that there are some oscillations in the q-axis suspension current as it has to lift-up the rotor from its initial position of [0,-0.5] in geometric co-ordinate terms. The oscillation settle down, indicating that the system is stabilizable.

Figure 21(c) and Figure 21(d) present the waveforms of the controlled rotor positions in x- and y-axes, respectively, during lifting up of the rotor. Due to the action of the controlled suspension currents, the rotor is able to follow its position references. However, no oscillations in the rotor position is observed.

Figure 21(e) and Figure 21(f) show the waveforms for the suspension forces in x- and y-axes. Oscillations in y-axis force are observed towards the beginning as it has to fight against the gravity to lift up the rotor. However, once the rotor starts following the desired rotor position references, such oscillations disappear.

Figure 22 demonstrates the controlled system responses to step input change and starting of the q-axis motor current. Figure 22(a) and Figure 22(b) present the rotor position waveforms in x- and y-axes respectively. The step input changes occur at different times for x- and y-axes positions. It can be observed that the rotor does follow its references here and the system does not become unstable. Moreover, step input change in one does not have any effect in the output of the other. Also, the starting of the q-axis motor current does not adversely affect the controlled rotor positions, which means that some sort of optimal decoupling has been achieved in this case.

Figure 22(c) and Figure 22(d) show the controlled d- and q-axes suspension currents. Some oscillations re-appear, after the initial lift-up, only when there are step input changes in the rotor positions. Furthermore, oscillations correlate to the individual step input changes in x- and y-axes rotor positions.

Figure 22(e) and Figure 22(f) present the suspension forces in x- and y-axes. They also exhibit some oscillations, albeit at different times, whenever there are step input changes in the rotor positions' references.

Finally, the figures for the step input and step output disturbances are plotted. Figure 23 demonstrates system responses to step input and output disturbances. Figure 23(a) and Figure 23(b) show the waveforms for the controlled rotor positions in x- and y-axes. It can be observed that there are minimal changes in the rotor positions during the step input disturbance, which is expressed as a fraction of the peak value of the suspension current. This conforms Figure 19 which reasonably high gains for the system at this junction. However, when performances to step output disturbances were investigated, the rotor positions go slightly off the desired rotor positions' references, which in turn, also conforms the marginally small gain exhibited by Figure 10. The controller did not show any tendency to bring the rotor back to its desired position references. The output disturbance is expressed as a fraction of the maximum allowable deviation from the central rotor position. It is observed that, system maintained stability when step input disturbance was within 47% of the peak value of suspension current and step output disturbance was within 55% of the maximum allowable deviation of the rotor from the central rotor position.

Figure 23(c) and Figure 23(d) present the controlled waveforms of the suspension currents in d- and q-axes. Oscillations are observed when step input disturbances were activated, but no such oscillations occur during step output disturbances. This further proves that controller did not function as desired during the time step output disturbances appeared. Figure 23(e) and Figure 23(f) show the waveforms of the suspension forces in x- and y-axes.

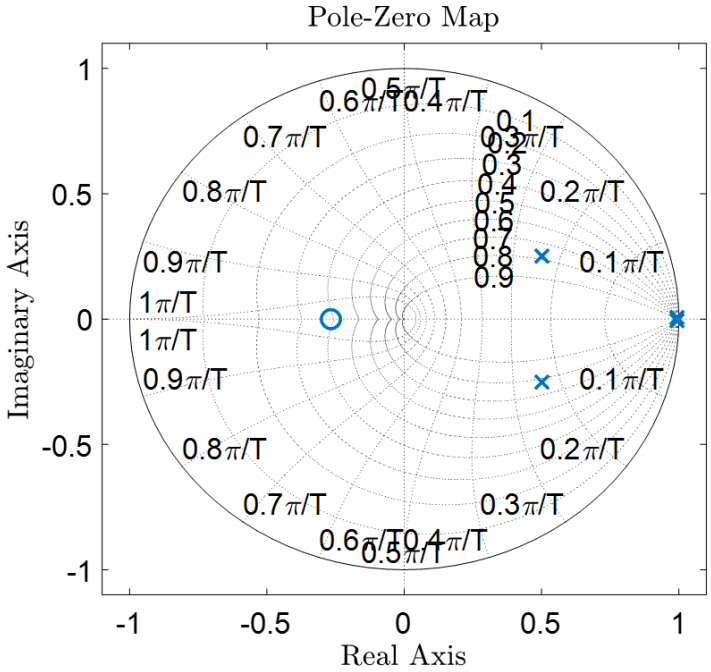

Figure 17: Pole-Zero Map of the System with Controller and State-Command path

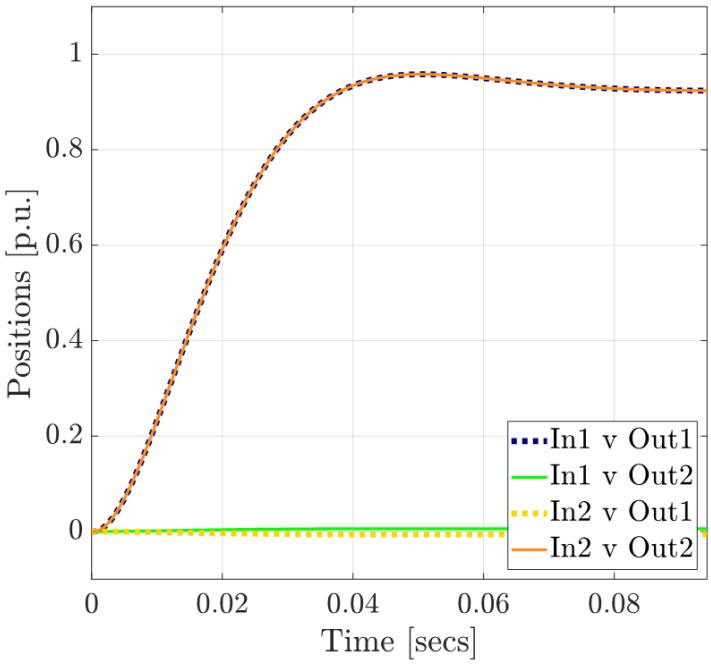

Figure 18: Step Response of the System with Controller and State-Command path

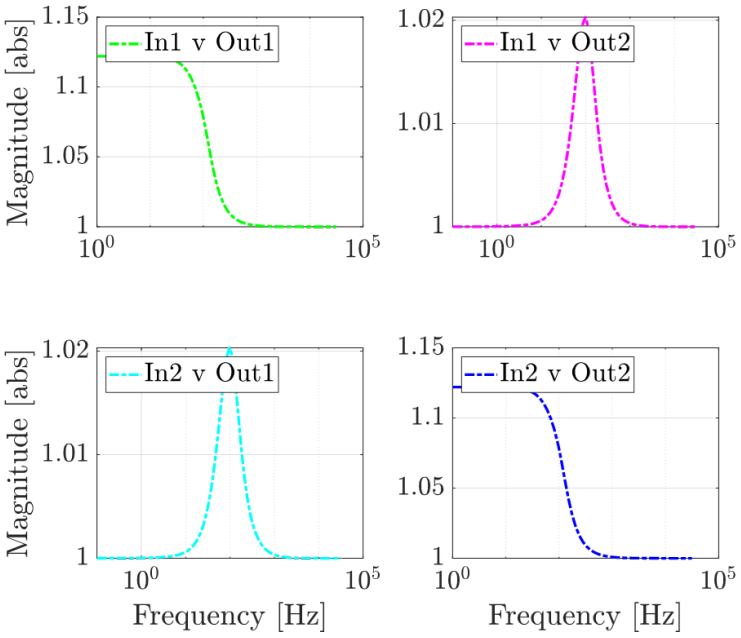

Figure 19: Reference-to-Error Sensitivity (Controller and State-command path)

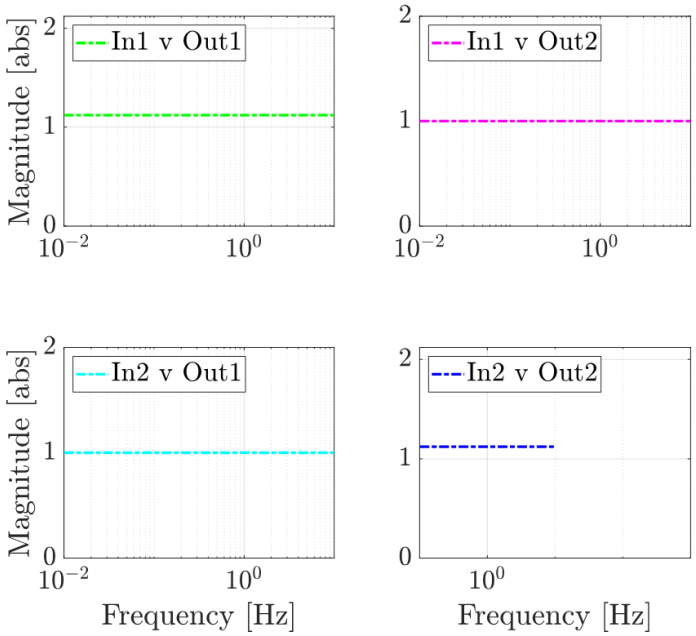

Figure 20: Output-Disturbance-to-Output Sensitivity (Controller and State-command path)

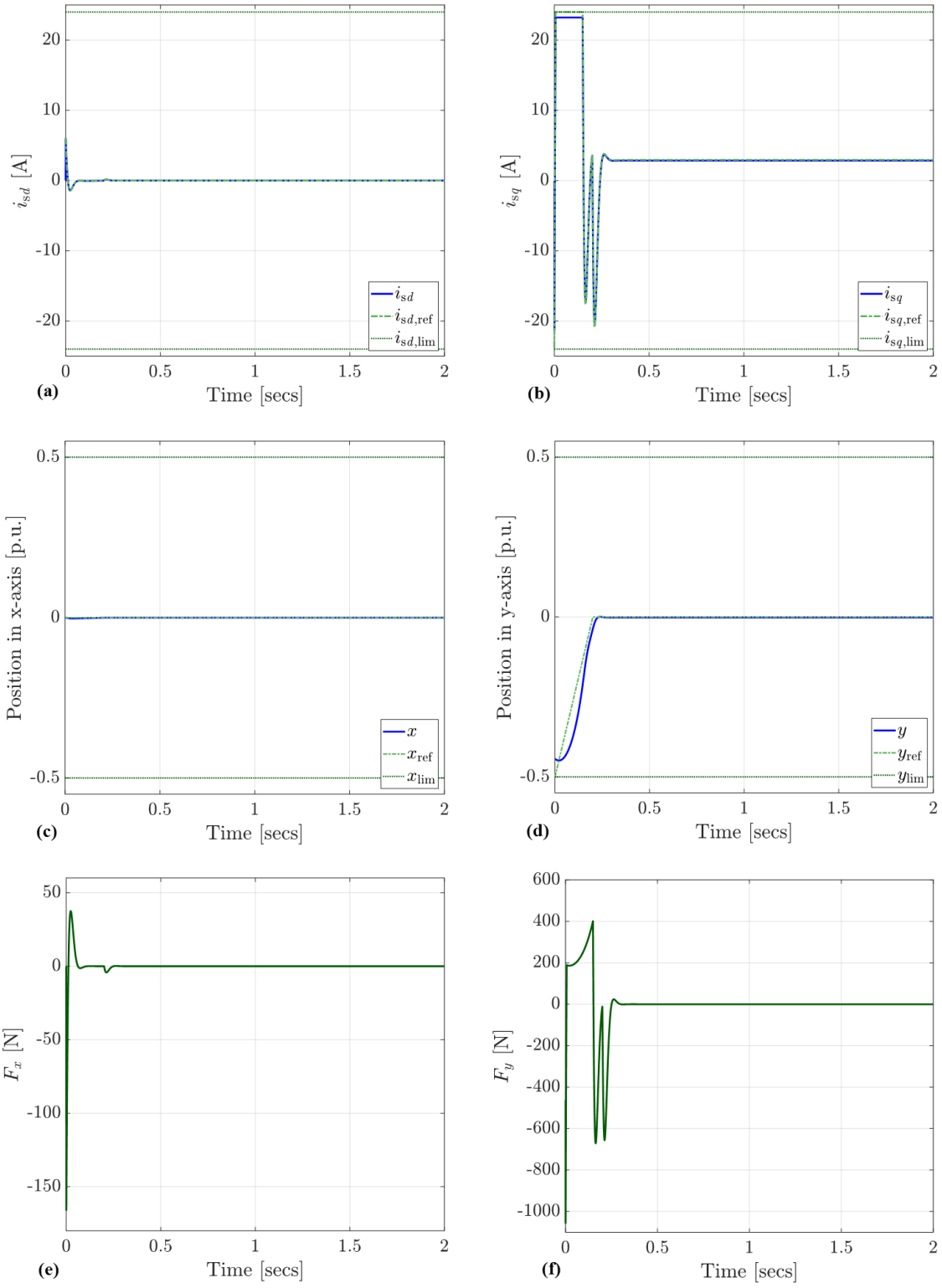

Figure 21: Rotor Lift-Up Dynamics (Controller with State-Command) – **(a)** Suspension current waveform in d-axis, **(b)** Suspension current waveform in q-axis, **(c)** x-axis rotor position, **(d)** y-axis rotor position, **(e)** Simulated suspension force waveform along x-axis, **(f)** Simulated suspension force waveform along y-axis

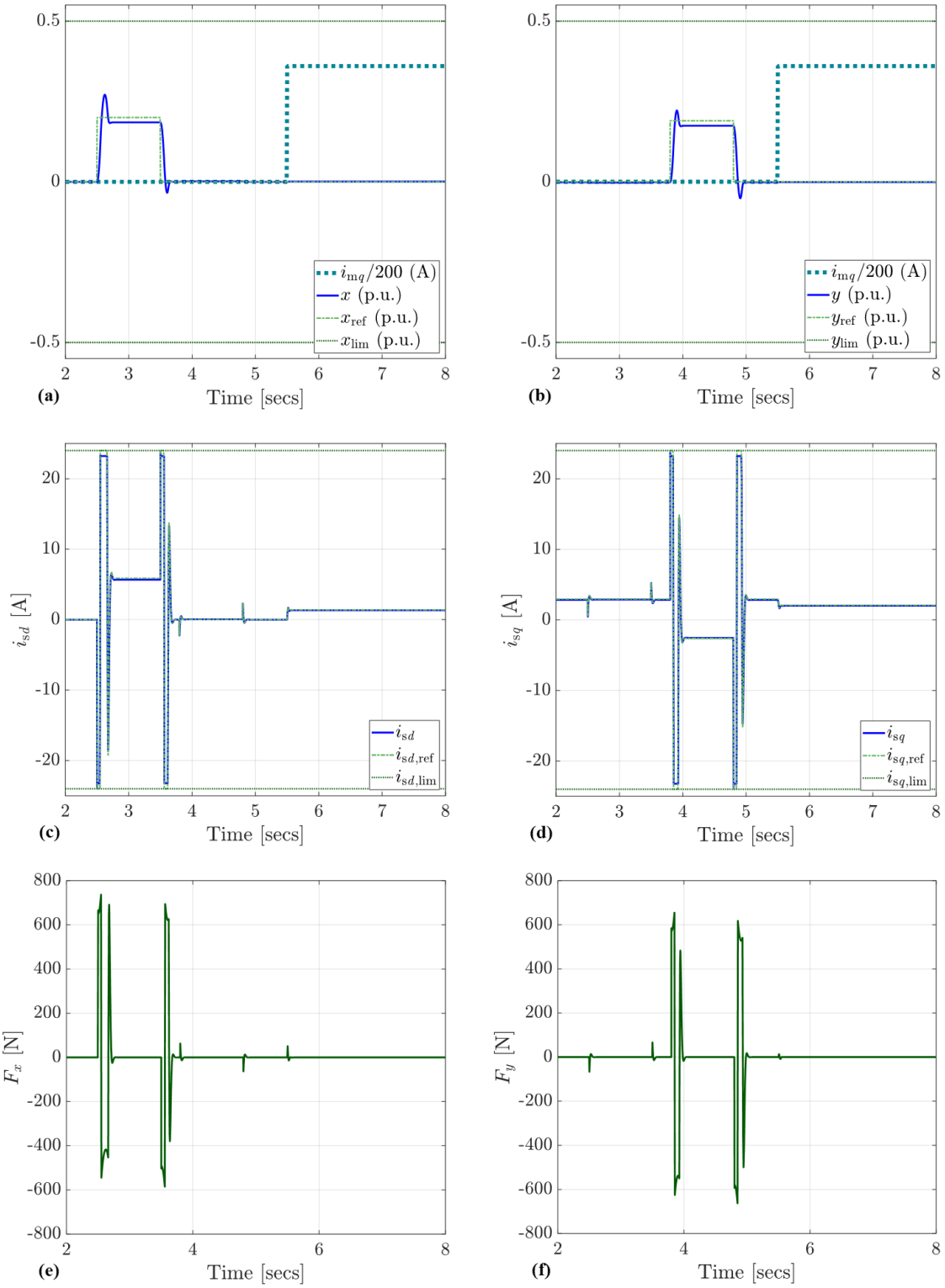

Figure 22: Step Change and Motor Current Dynamics (Controller with State-Command) – **(a)** x-axis rotor position, **(b)** y-axis rotor position, **(c)** Suspension current waveform in d-axis, **(d)** Suspension current waveform in q-axis, **(e)** Simulated suspension force waveform along x-axis, **(f)** Simulated suspension force waveform along y-axis

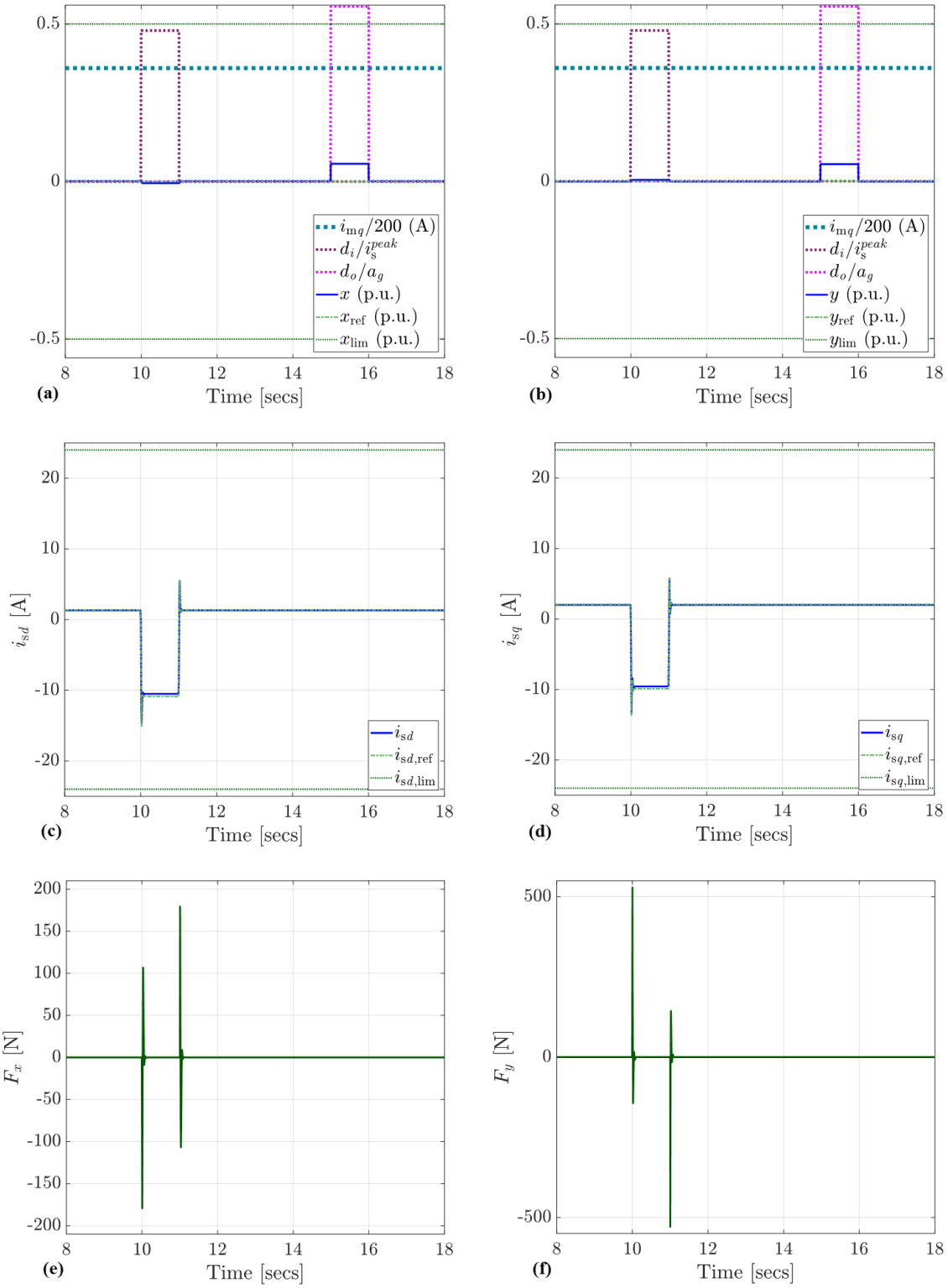

Figure 23: Step Input and Output Disturbances Dynamics (Controller with State-Command) – **(a)** x-axis rotor position, **(b)** y-axis rotor position, **(c)** Suspension current waveform in d-axis, **(d)** Suspension current waveform in q-axis, **(e)** Simulated suspension force waveform along x-axis, **(f)** Simulated suspension force waveform along y-axis

4 Kalman Estimator

4.1 Controller and Estimator

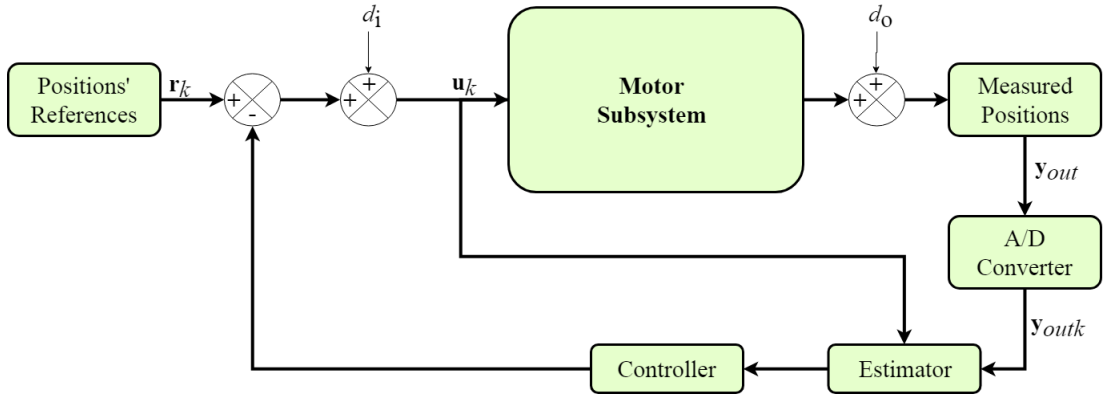

Figure 24: Controlled System's Structure with Controller and Estimator

It would be pretty unrealistic to assume that all the states can be measured, especially when it is widely known that no process can ever be free from even the slightest of disturbances. Hence, an estimator will invariably come in handy in our case. This estimator will be capable of not only estimating unmeasured states, if any, but also filtering out non-desirable noises, both at the process input and output, indicated by d_i and d_o in Figure 24 which gives the desired structure for the controlled system with controller and estimator. The system will have to be, in that case, observable. The observability matrix $\mathbf{W}_\mathrm{o} = [\mathbf{C}^\mathrm{T}\ \mathbf{F}^\mathrm{T}\mathbf{C}^\mathrm{T}\ (\mathbf{F}^2)^\mathrm{T}\mathbf{C}^\mathrm{T}\ \ldots\ (\mathbf{F}^{n-1})^\mathrm{T}\mathbf{C}^\mathrm{T}]^\mathrm{T}$ also has a full rank for this system.

One of the biggest benefits of using an estimator is that it will be able to do the estimation of the states $\mathbf{x}_\mathrm{pu}(k)$, at k^{th} sampling, based on the past and present values of $\mathbf{u}_\mathrm{pu}$ and $\mathbf{y}_\mathrm{outpu}$ ($\mathbf{u}_\mathrm{pu}(k)$, $\mathbf{u}_\mathrm{pu}(k-1)$, ..., $\mathbf{y}_\mathrm{outpu}(k)$, $\mathbf{y}_\mathrm{outpu}(k-1)$). The availability of the system model will quicken the purpose. The estimator will take feedback from the output and continuously compare it with the reference inputs.

For this system, Kalman Estimator is used in order to get the values for the estimator matrix $\mathbf{L}$. The output is continuously compared with the states and the errors are thus continuously minimized. Another thing is that per-unit matrices have been used for our calculations. However here the notations related to non-per-unit system are used for the reader's easy comprehension.

The noises may appear at the process as well as the measurement side. $\mathbf{F}$ and $\mathbf{G}$ are discrete equivalents of $\mathbf{A}$ and $\mathbf{B}$, respectively. In that case the state-space representation of the system can be given as

$$\mathbf{x}_{k+1} = \mathbf{F}\mathbf{x}_k + \mathbf{G}\mathbf{u}_k + \mathbf{G}_\mathrm{n}\mathbf{w}_k$$

$$\mathbf{y}_k = \mathbf{C}\mathbf{x}_k + \mathbf{D}\mathbf{u}_k + \mathbf{H}_\mathrm{n}\mathbf{w}_k + \mathbf{v}_k$$

where, $\mathbf{w}_k$ is the Gaussian zero-mean process noise, $\mathbf{v}_k$ is the Gaussian zero-mean measurement noise, $\mathbf{G}_\mathrm{n}$ is the process-to-state noise matrix and $\mathbf{H}_\mathrm{n}$ is the process-to-measurement noise matrix. The co-variances of the noises are given as

$$\mathbf{R}_w = E\Big[\mathbf{w}_k\mathbf{w}_k^\mathrm{T}\Big]$$

$$\mathbf{R}_v = E\Big[\mathbf{v}_k\mathbf{v}_k^\mathrm{T}\Big]$$

$$\mathbf{R}_{wv} = E\Big[\mathbf{w}_k\mathbf{v}_k^\mathrm{T}\Big]$$

where, $\mathbf{R}_w$ is the process noise co-variance matrix, $\mathbf{R}_v$ is the measurement noise co-variance matrix and $\mathbf{R}_{wv}$ is the process-measurement noise co-variance matrix. The Riccati equation for Kalman estimation can now be given by

$$\mathbf{L} = (\mathbf{FPC}^\mathrm{T} + \overline{\mathbf{R}}_{wv})(\mathbf{CPC}^\mathrm{T} + \overline{\mathbf{R}}_v)^{-1}$$

where, $\mathbf{P}_{(k+1|k)} = \mathbf{R}_w + \mathbf{FP}_{(k|k-1)}\mathbf{F}^\mathrm{T} - \mathbf{FP}_{(k|k-1)}\mathbf{C}_\mathrm{T}\Big[\mathbf{CP}_{(k|k-1)} + \mathbf{R}_v\Big]\mathbf{CP}_{(k|k-1)}\mathbf{F}_\mathrm{T}$[26], $\overline{\mathbf{R}}_v = \mathbf{R}_v + \mathbf{H}_\mathrm{n}\mathbf{R}_{wv} + \mathbf{R}_{wv}^\mathrm{T}\mathbf{H}_\mathrm{n}^\mathrm{T} + \mathbf{H}_\mathrm{n}\mathbf{Q}\mathbf{H}_\mathrm{n}^\mathrm{T}$ and $\overline{\mathbf{R}}_{wv} = \mathbf{G}_\mathrm{n}(\mathbf{Q}\mathbf{H}_\mathrm{n}^\mathrm{T} + \mathbf{R}_{wv})$. $\mathbf{P}$ is the solution to Riccati equation. The estimated states for the system, together with controller and estimator can be expressed as

$$\begin{aligned}
\hat{\mathbf{x}}_{k+1} &= \mathbf{F}\hat{\mathbf{x}}_k + \mathbf{G}\mathbf{u}_k + \mathbf{L}(\mathbf{y}_{\mathrm{out}k} - \mathbf{C}\hat{\mathbf{x}}_k)\Big[\hat{\mathbf{x}}_k = \text{estimated states in discrete time}\Big] \\
&= \mathbf{F}\hat{\mathbf{x}}_k + \mathbf{G}(-\mathbf{K}\hat{\mathbf{x}}_k + \mathbf{r}_k) + \mathbf{L}\mathbf{y}_{\mathrm{out}k} - \mathbf{LC}\hat{\mathbf{x}}_k \\
&= \mathbf{F}\hat{\mathbf{x}}_k - \mathbf{GK}\hat{\mathbf{x}}_k + \mathbf{G}\mathbf{r}_k + \mathbf{LC}\mathbf{x}_k - \mathbf{LC}\hat{\mathbf{x}}_k \ \ [\because \mathbf{y}_{\mathrm{out}k} = \mathbf{C}\mathbf{x}_k] \\
&= (\mathbf{LC})\mathbf{x}_k + (\mathbf{F} - \mathbf{GK} - \mathbf{LC})\hat{\mathbf{x}}_k + (\mathbf{G})\mathbf{r}_k \\
\text{or, } \hat{\mathbf{x}}_{k+1} &= \begin{bmatrix}\mathbf{LC} & (\mathbf{F} - \mathbf{GK} - \mathbf{LC})\end{bmatrix}\begin{bmatrix}\mathbf{x}_k \\ \\ \hat{\mathbf{x}}_k\end{bmatrix} + \begin{bmatrix}\mathbf{G}\end{bmatrix}\mathbf{r}_k
\end{aligned} \tag{25}$$

The closed-loop system, together with the controller and estimator, can be written as

$$\begin{aligned}
\mathbf{x}_{k+1} &= \mathbf{F}\mathbf{x}_k + \mathbf{G}\mathbf{u}_k \\
&= \mathbf{F}\mathbf{x}_k + \mathbf{G}(-\mathbf{K}\hat{\mathbf{x}}_k + \mathbf{r}_k) \\
&= \mathbf{F}\mathbf{x}_k - \mathbf{GK}\hat{\mathbf{x}}_k + \mathbf{G}\mathbf{r}_k
\end{aligned} \tag{26}$$

Hereafter, our system is augmented using the above control law and the estimated states. The dynamics of such a system will contain poles and zeroes from both controller and estimator. The augmented system is written as

$$\begin{bmatrix}\mathbf{x}_{k+1} \\ \hat{\mathbf{x}}_{k+1}\end{bmatrix} = \begin{bmatrix}\mathbf{F} & -\mathbf{GK} \\ \\ \mathbf{LC} & \underbrace{(\mathbf{F} - \mathbf{GK} - \mathbf{LC})}_{\mathbf{F}_\mathrm{c}}\end{bmatrix}\begin{bmatrix}\mathbf{x}_k \\ \\ \hat{\mathbf{x}}_k\end{bmatrix} + \begin{bmatrix}\mathbf{G} \\ \\ \mathbf{G}\end{bmatrix}\mathbf{r}_k \tag{27}$$

Bryson's rule[26] is also applied here. It is assumed that the Root-Mean-Square (RMS) accuracy of the position measurements is 0.02 mm. With this assumption in place, the measurement noise matrix $\mathbf{R}_v$ for the estimator can be written as

$$\mathbf{R}_v = \begin{bmatrix} (0.02)^2 & 0 \\ 0 & (0.02)^2 \end{bmatrix} \tag{28}$$

Generally, choosing the values for process noise matrix $\mathbf{R}_w$ cannot be done with the same degree of certainty or precision unlike $\mathbf{R}_v$. For the system, it is assumed that the input disturbances enter the system identical to i_{sd} and i_{sq}. Measurements of the input current are necessary to determine the accurate values of $\mathbf{R}_w$. However, disturbances and some modelling errors can also adversely impact the system and need to be quantified in order to arrive at a truly optimal estimator. For these reasons, the initial diagonal entries for $\mathbf{R}_w$ are arbitarily picked here. The estimator gains and resulting roots are then computed. $\mathbf{R}_w$ is then modified, based on the estimator performance in simulations including measurement noise and other not-accounted-for disturbances. The initial diagonal entires for $\mathbf{R}_w$ are

$$\mathbf{R}_w = \begin{bmatrix} 0.0001 & 0 \\ 0 & 0.0001 \end{bmatrix} \tag{29}$$

Figure 25 shows the pole-zero map of the system with controller and estimator. Comparing this figure with Figure 7, it can be observed that there is an additional zero inside the unit circle due to addition of estimator here. Figure 26 shows the step response of the same system. The steady-state errors are present. Moreover, faster dynamics are observed which forebode loss of stability for the controlled suspension currents. Figure 27 and Figure 28 show the reference-to-error and output-disturbances-to-output sensitivities. It can be predicted from these two figures that the system *will* lose stability if disturbances were to appear at the junctions reference-to-system and system-to-output. For verification purposes, simulations of the system with controller and estimation were run and waveforms for those are also provided.

Figure 29 demonstrates the rotor lift-up dynamics of the controlled system with controller and estimator. Figure 29(a) and Figure 29(b) show the controlled suspension current waveforms in d- and q-axes respectively. Oscillations occur in order to bring the rotor position to its desired central position, given by [0,0] in geometric co-ordinate terms.

Figure 29(c) and Figure 29(d) present the rotor position waveforms in the x- and y-axes. Steady-state errors are clearly visible. These sorts of performance were already prophesized by Figure 26, where it was observed that fast dynamics and steady-state errors are present. Since the steady-state errors exist in the estimator, the rotor does not follow its position references because in this controlled system, controller is fed with the estimation of rotor positions and not with the states of the system. Hence, those errors linger behind and show up during the lifting up of the rotor.

Figure 30 demonstrates the controlled system's responses to step input change and starting of the q-axis motor current. Figure 30(a) and Figure 30(b) show the rotor's positions in x- and y-axes, respectively, during the same. Hardly any changes could be perceived in rotor's x- and y-axes' positions due to step input change which correlates with Figure 26. The steady-state errors are also present here. The controlled system moves further towards unstability once the q-axis motor current is started, which is quite in line with Figure 26.

Finally, Figure 31 demonstrates the controlled system responses to step input and step output disturbances, which are also expressed here as fraction of the peak value of suspension current and fraction of the maximum allowable deviation of the rotor position from its central position, respectively. Figure 31(a) and Figure 31(b) show the controlled system's rotor positions in x- and y-axes, respectively, when step input and output disturbances appear at the reference-to-system and system-to-output junctions. The system loses its stability as soon as the input disturbances appear, because of which, it is already unresponsive by the time output disturbances appear. Such waveforms *do* fall in line with Figure 27 and Figure 28 where the gains start to misbehave at higher frequencies.

The suspension currents in d- and q-axes in Figure 31(c) and Figure 31(d) also become unstable. The effects of the unstability are also felt on the suspension forces generated by the permanent magnets and shown in Figure 31(e) and Figure 31(f).

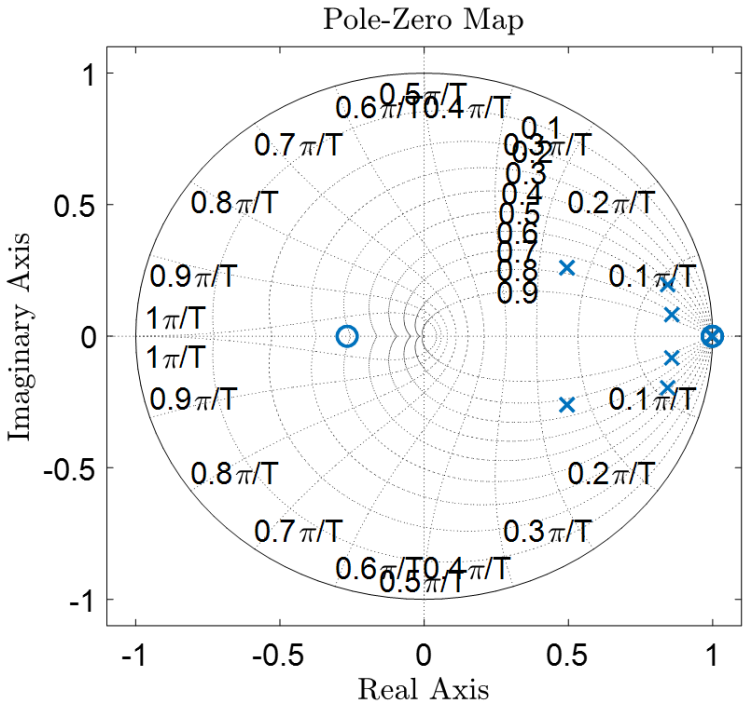

Figure 25: Pole-Zero Map of the System with Controller and Estimator

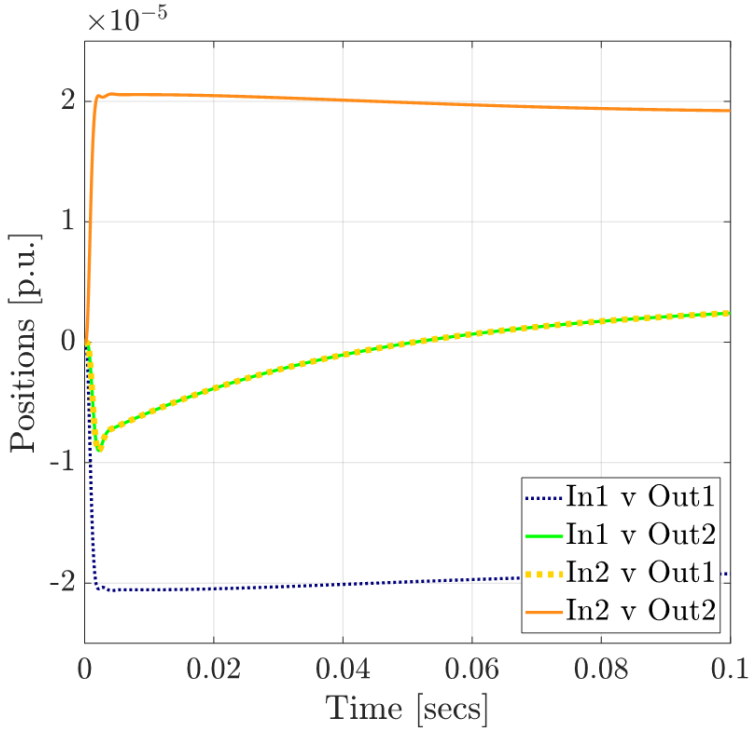

Figure 26: Step Response of the System with Controller and Estimator

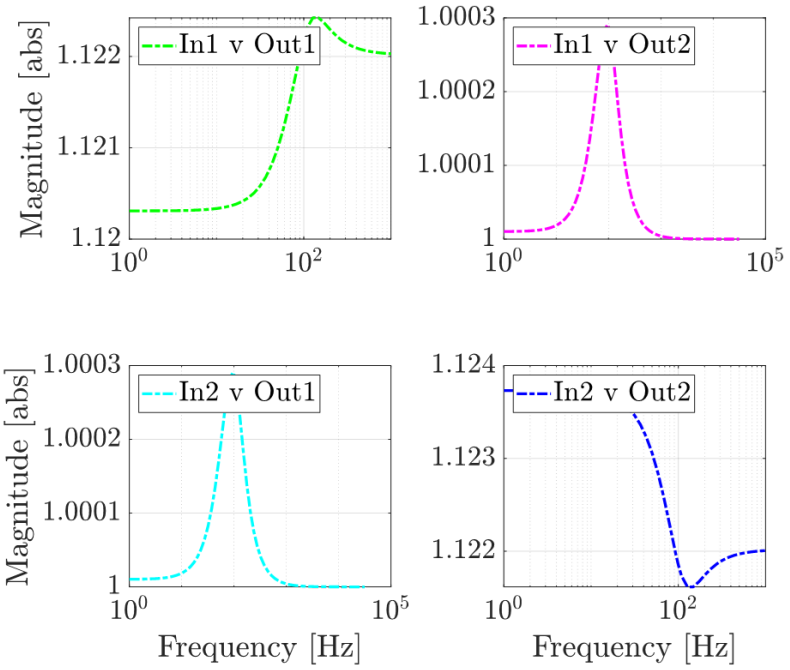

Figure 27: Reference-to-Error Sensitivity (Controller and Estimator)

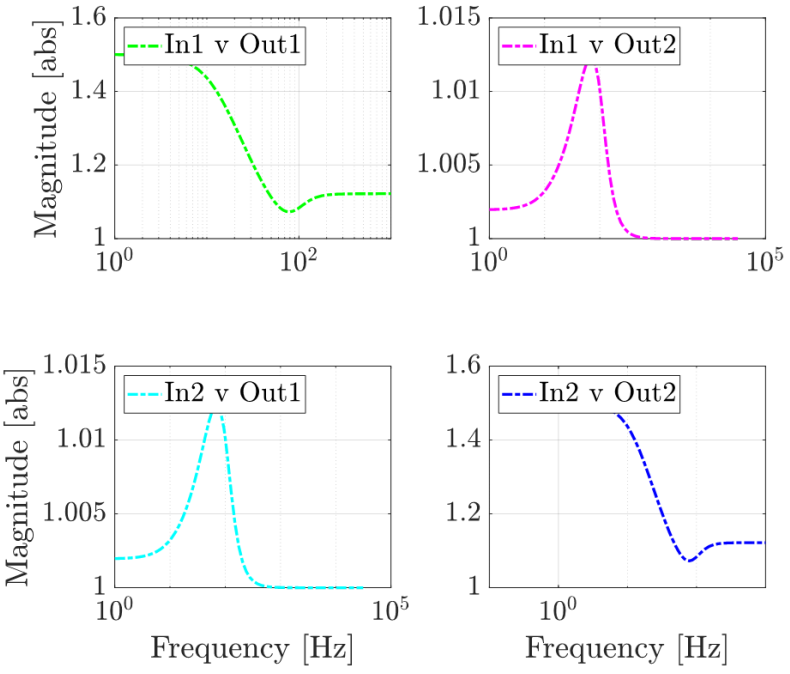

Figure 28: Output-Disturbances-to-Output Sensitivity (Controller and Estimator)

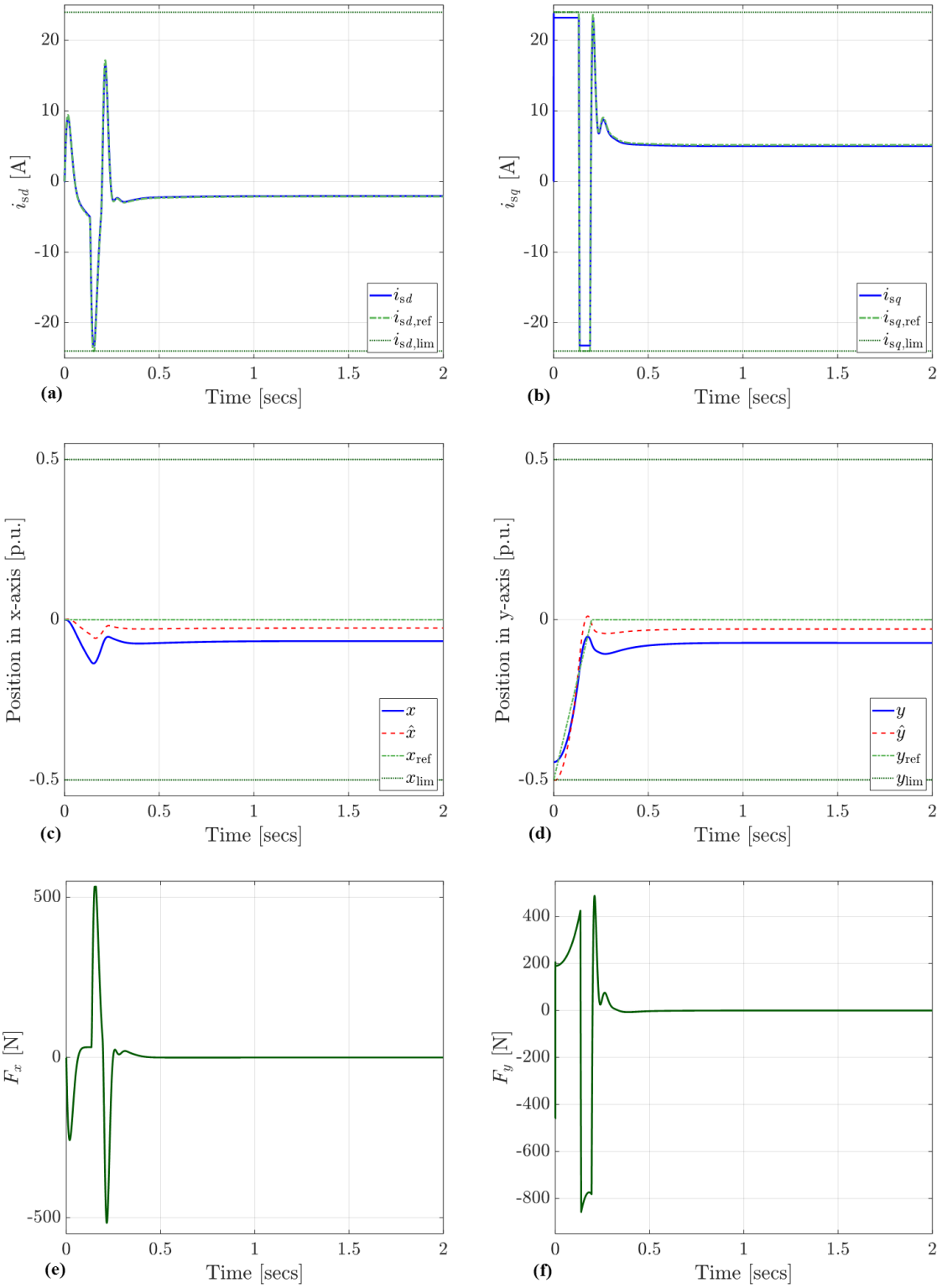

Figure 29: Rotor Lift-Up Dynamics (Controller and Estimator) – **(a)** Suspension current waveform in d-axis, **(b)** Suspension current waveform in q-axis, **(c)** x-axis rotor position, **(d)** y-axis rotor position, **(e)** Simulated suspension force waveform along x-axis, **(f)** Simulated suspension force waveform along y-axis

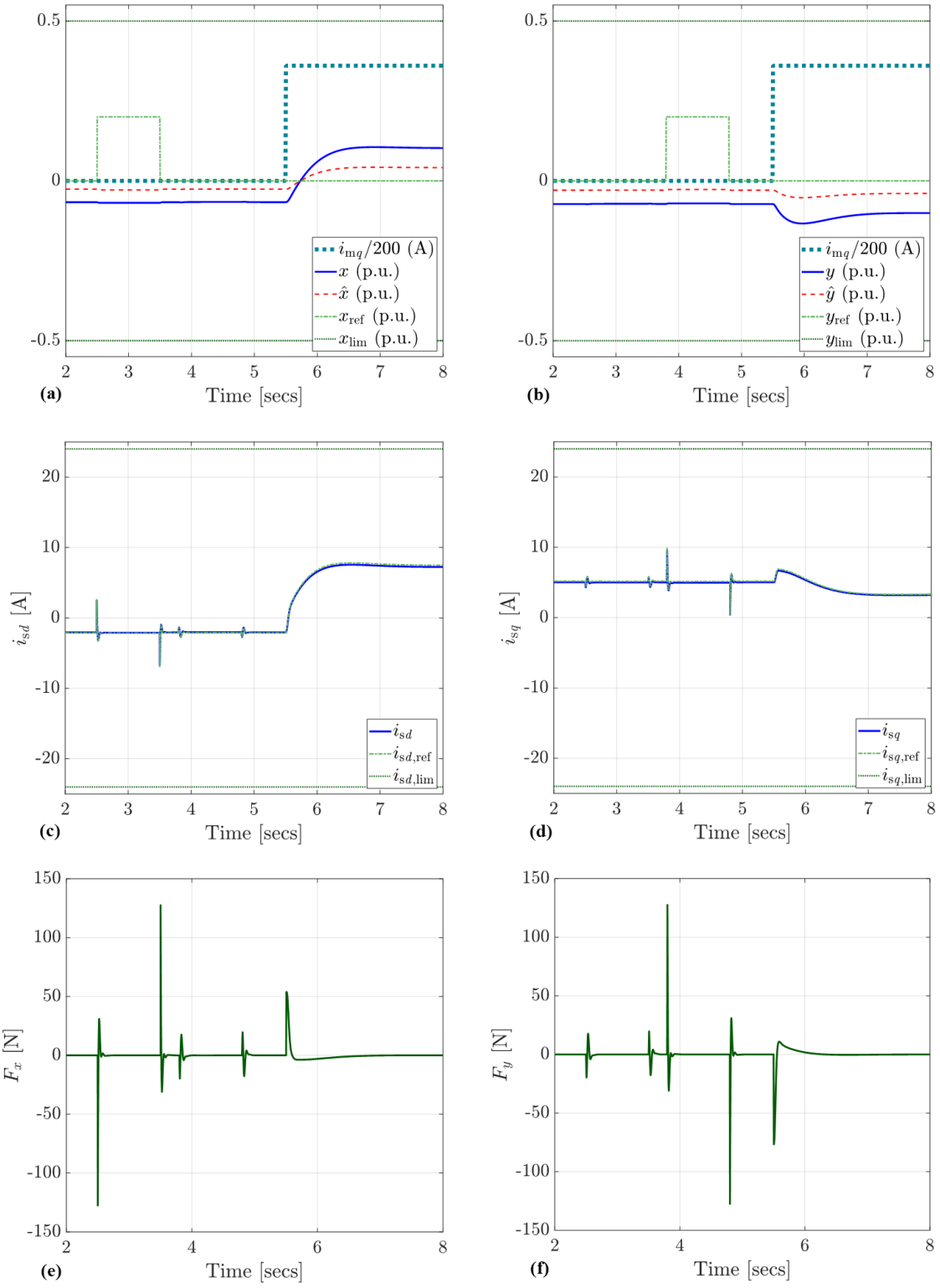

Figure 30: Step Change and Motor Current Dynamics (Controller and Estimator) – **(a)** x-axis rotor position, **(b)** y-axis rotor position, **(c)** Suspension current waveform in d-axis, **(d)** Suspension current waveform in q-axis, **(e)** Simulated suspension force waveform along x-axis, **(f)** Simulated suspension force waveform along y-axis

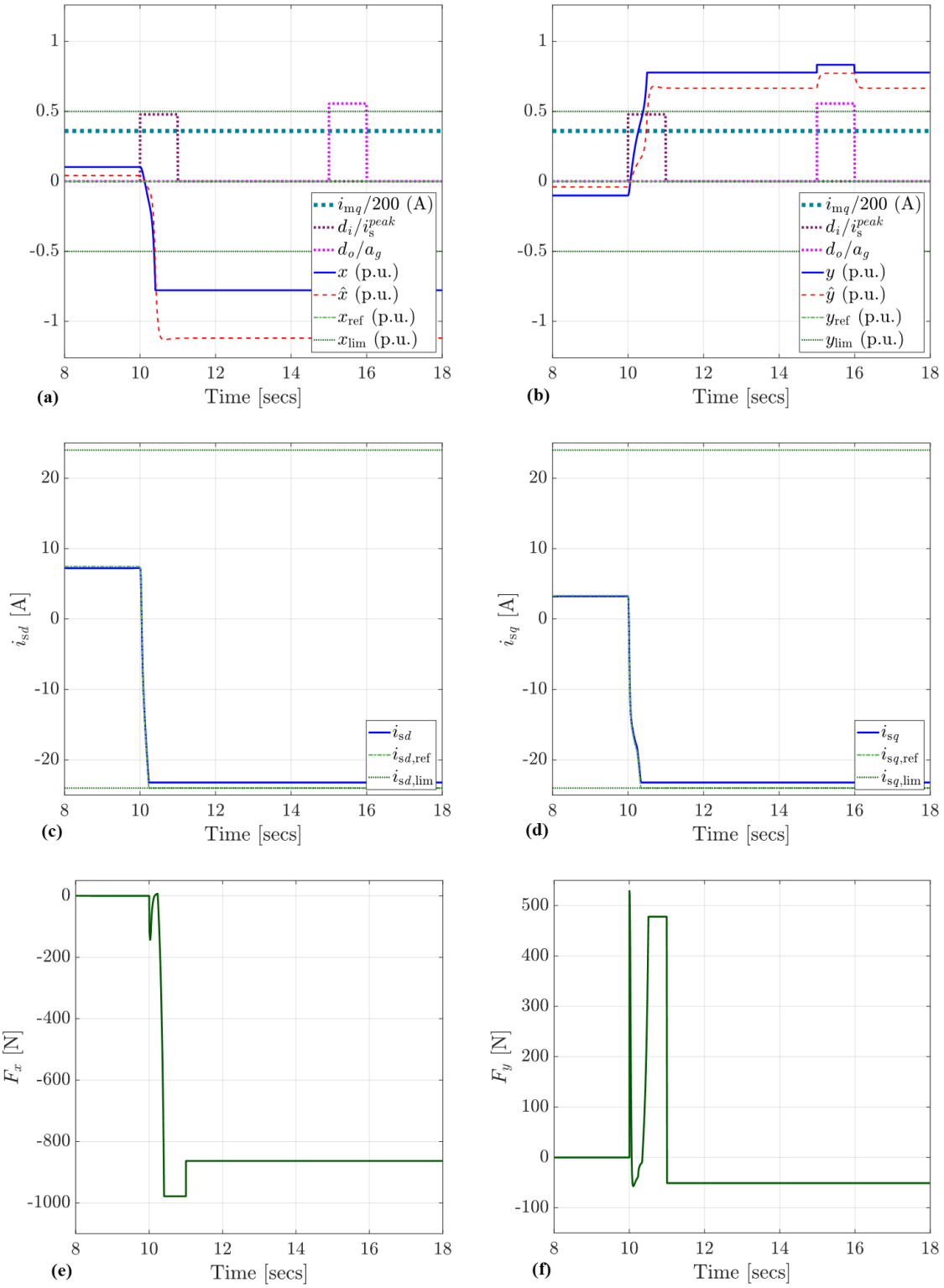

Figure 31: Step Input and Output Disturbances Dynamics (Controller and Estimator) – **(a)** x-axis rotor position, **(b)** y-axis rotor position, **(c)** Suspension current waveform in d-axis, **(d)** Suspension current waveform in q-axis, **(e)** Simulated suspension force waveform along x-axis, **(f)** Simulated suspension force waveform along y-axis

4.2 Controller with State-command Path and Estimator

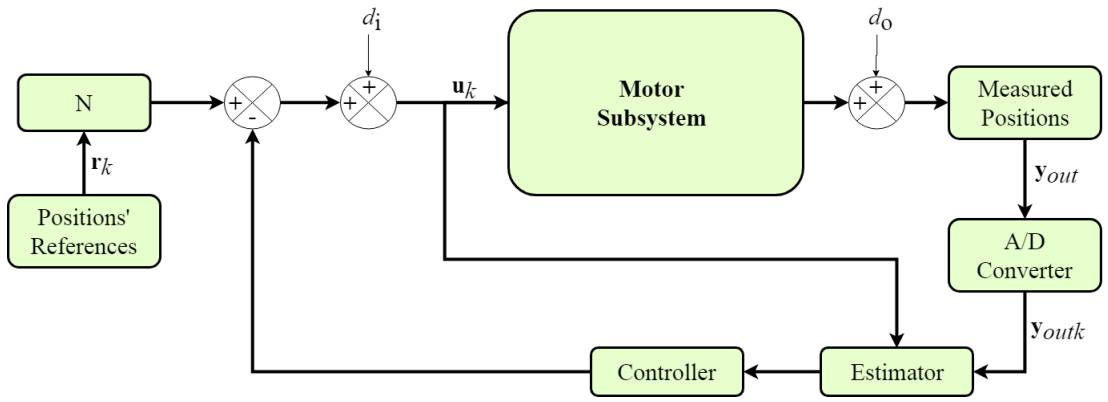

Figure 32: Controlled System's Structure with Controller, State-command and Estimator

The system is now fitted with a controller that includes a state-command path and an estimator. The reason behind trying out this control strategy is to check whether the dynamics of the system are improved or not. The stability of the controlled system was lost as soon as input disturbances appeared at the reference-to-system junction. Hence, this control strategy is now implemented. The state-command matrix $\mathbf{N}$ is computed in the same fashion as it was done before. The augmented system can now be given by

$$\begin{bmatrix} \mathbf{x}_{k+1} \\ \hat{\mathbf{x}}_{k+1} \end{bmatrix} = \begin{bmatrix} \mathbf{F} & -\mathbf{GK} \\ \mathbf{LC} & (\mathbf{F} - \mathbf{GK} - \mathbf{LC}) \end{bmatrix} \begin{bmatrix} \mathbf{x}_k \\ \hat{\mathbf{x}}_k \end{bmatrix} + \begin{bmatrix} \mathbf{GN} \\ \mathbf{GN} \end{bmatrix} \mathbf{r}_k \tag{30}$$

Figure 33 shows the pole-zero map of the system where controller with state-command path and estimator are used. Some of the poles over here also lie perilously close to the border of the unit circle, which indicates that system may become unstable again if disturbances appear. Figure 34 present the step response of the controlled system. Over here, for a step change of magnitude 0.2, there are no steady-state errors, which indicates that the system will respond to step changes for this controlled system, which was basically absent from the controlled system with controller and estimator only. And finally, looking at the sensitivities, given by Figure 35 and Figure 36, the system exhibits conservatism once again, which indicate that for higher frequencies, if there are disturbances, the system *will* become unstable.

Coming to the dynamics of the controlled system, Figure 37(a) and Figure 37(b) show the controlled suspension current waveforms. Oscillations are still there, just like in Figure 29(a) and Figure 29(b). No major changes could be found in the rotor position waveforms given by Figure 37(c) and Figure 37(d).

However, some changes *are* there in the rotor position waveforms, given by Figure 38(a) and Figure 38(b). When the system is fitted with a controller that contains state-command path, the controlled system does start to respond to step changes in the input. This was already indicated by Figure 34 and is now proven during the dynamics investigation.

However, having said that, the system does become unstable when disturbances appear at the junction like reference-to-system and system-to-output. Such was already predicted by Figure 35 and Figure 36 and now confirmed by Figure 39(a) and Figure 39(b).

Almost all the control strategies, except one, which have been hitherto tested contain some sort of instability, excpet the control strategy developed with controller and state-command path. Hence, control strategies, which additionally include error integral, will now be investigated next. The overall system control analyses will again be investigated and the dynamics will be plotted.

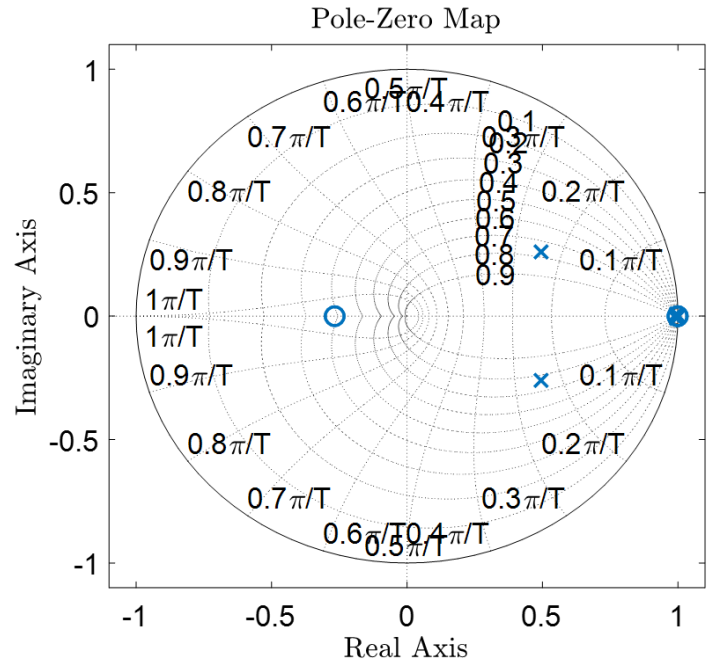

Figure 33: Pole-Zero Map of the System with Controller, State-command Path and Estimator

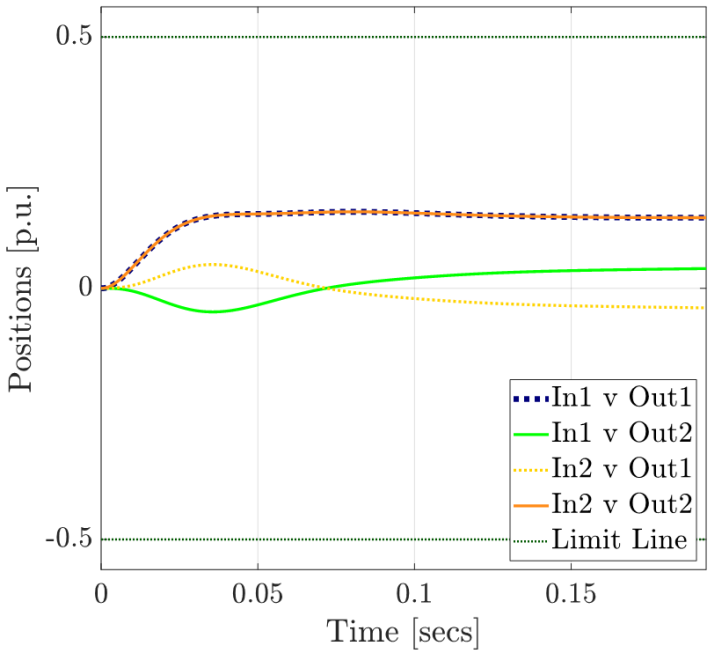

Figure 34: Step Response of the System with Controller, State-command Path and Estimator

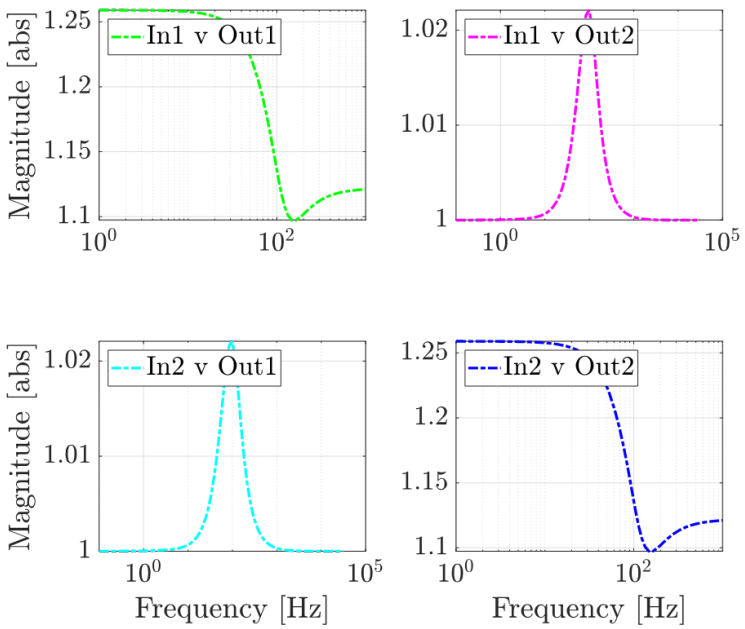

Figure 35: Reference-to-Error Sensitivity (Controller, State-command Path and Estimator)

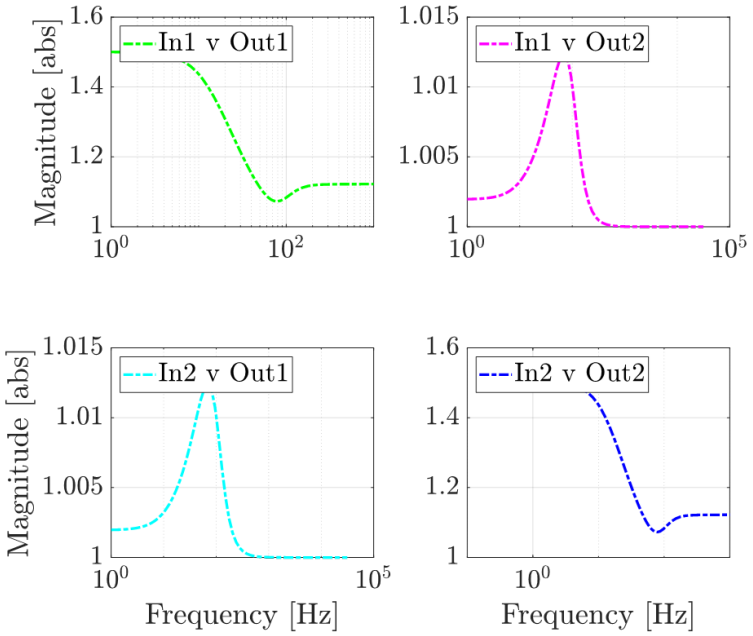

Figure 36: Output-Disturbances-to-Output Sensitivity (Controller, State-command Path and Estimator)

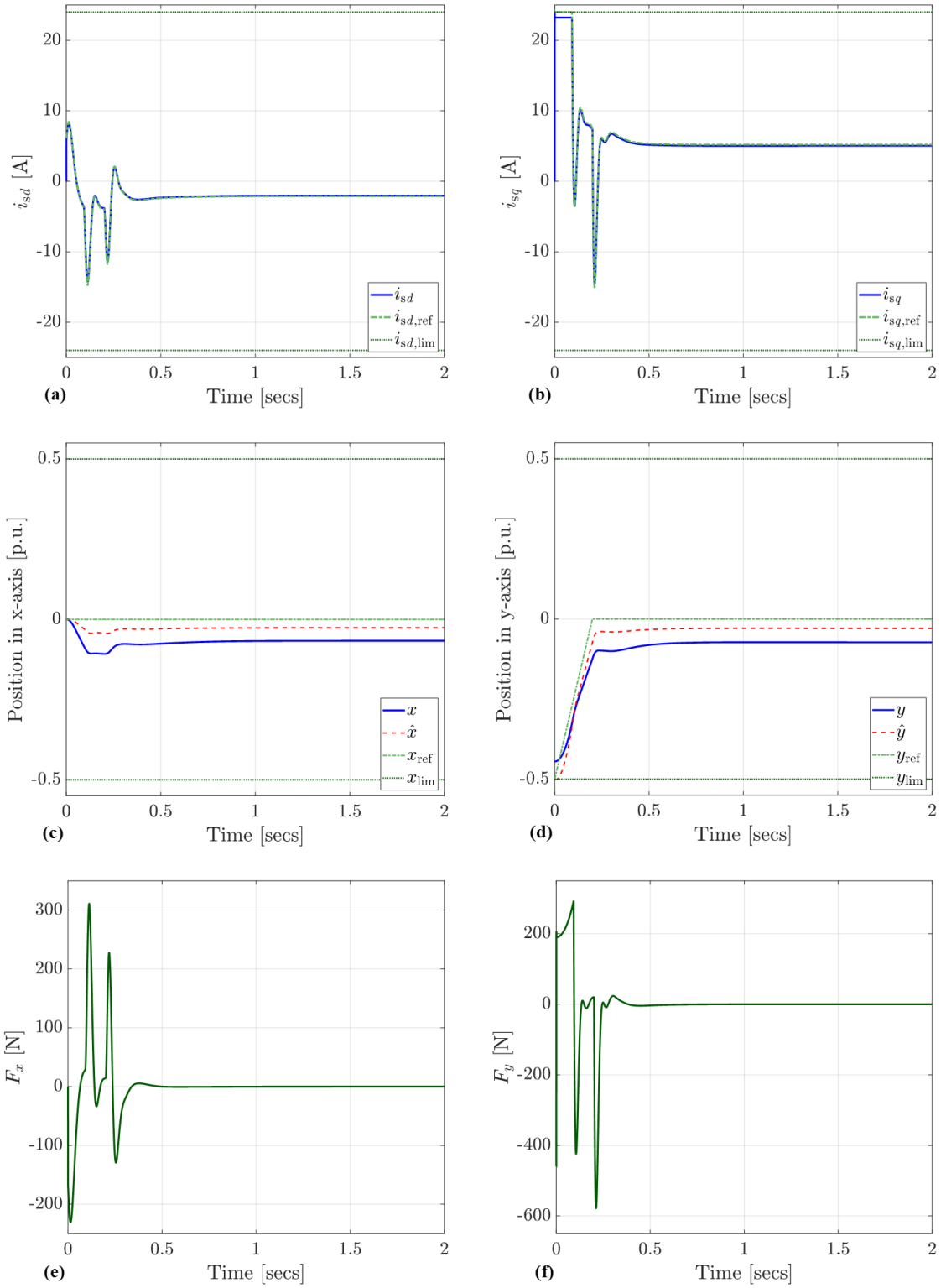

Figure 37: Rotor Lift-Up Dynamics (Controller, State-command Path and Estimator) – **(a)** Suspension current waveform in d-axis, **(b)** Suspension current waveform in q-axis, **(c)** x-axis rotor position, **(d)** y-axis rotor position, **(e)** Simulated suspension force waveform along x-axis, **(f)** Simulated suspension force waveform along y-axis

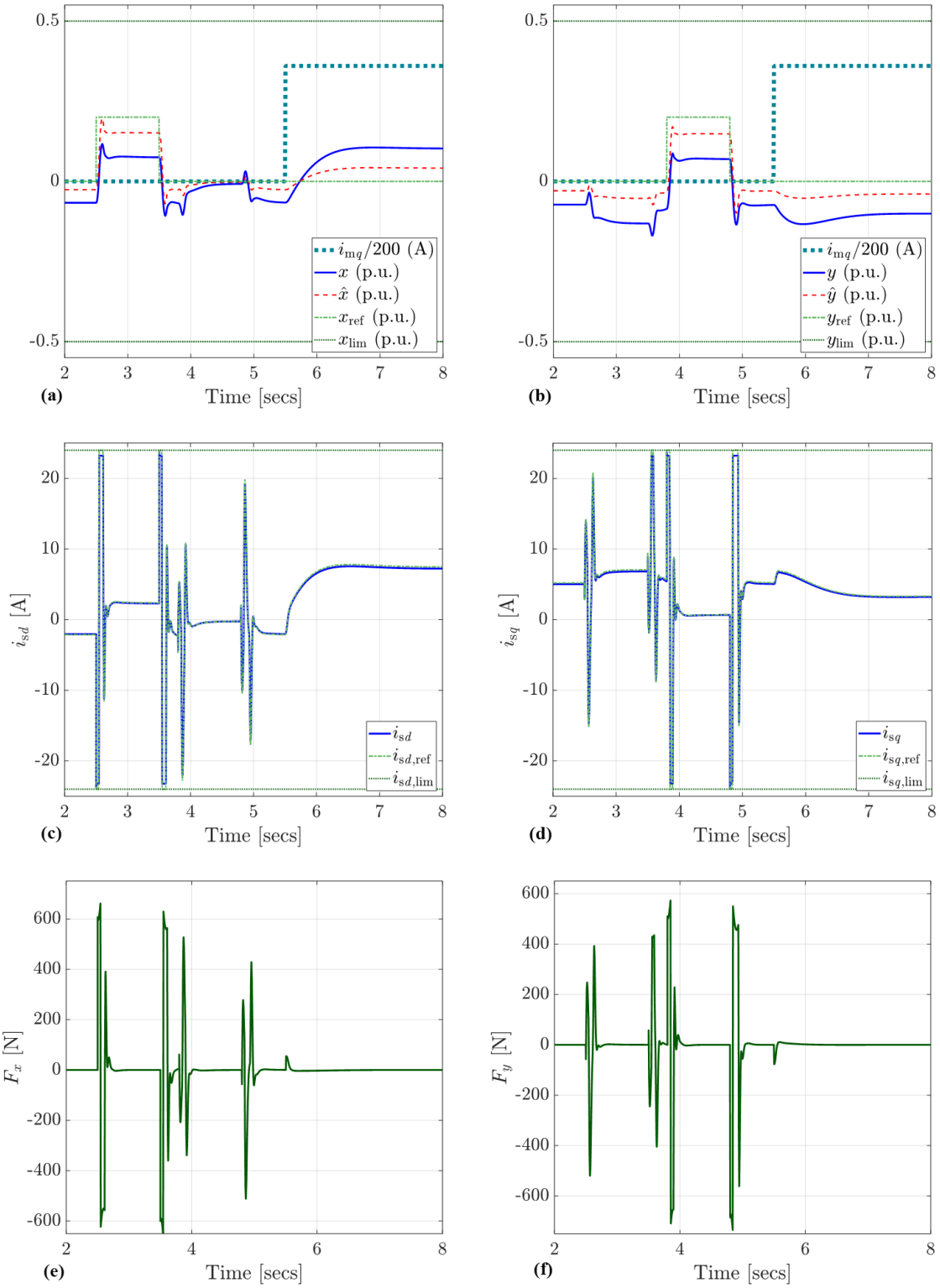

Figure 38: Step Change and Motor Current Dynamics (Controller, State-command Path and Estimator) – **(a)** x-axis rotor position, **(b)** y-axis rotor position, **(c)** Suspension current waveform in d-axis, **(d)** Suspension current waveform in q-axis, **(e)** Simulated suspension force waveform along x-axis, **(f)** Simulated suspension force waveform along y-axis

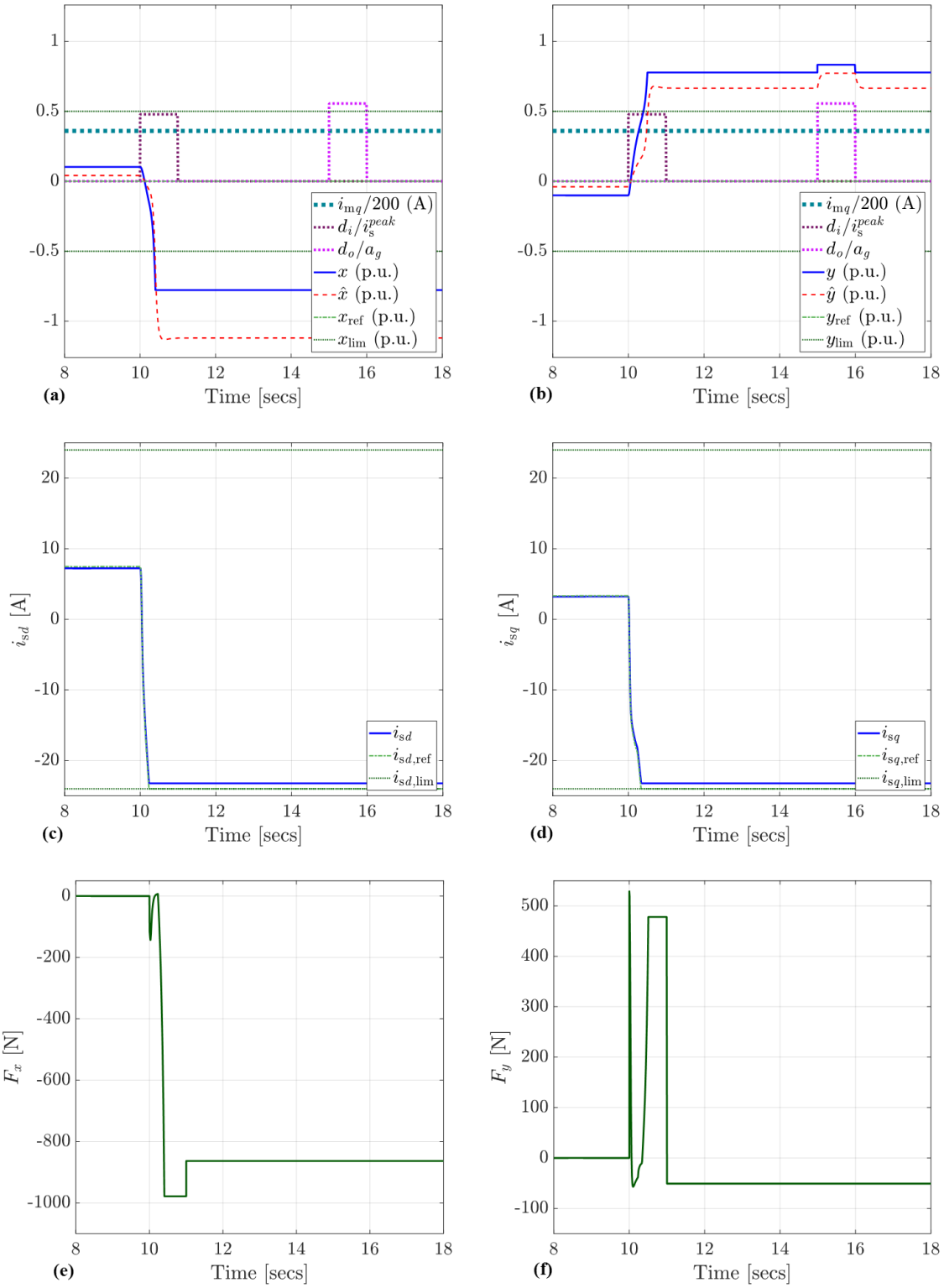

Figure 39: Step Input and Output Disturbances Dynamics (Controller, State-command Path and Estimator) – **(a)** x-axis rotor position, **(b)** y-axis rotor position, **(c)** Suspension current waveform in d-axis, **(d)** Suspension current waveform in q-axis, **(e)** Simulated suspension force waveform along x-axis, **(f)** Simulated suspension force waveform along y-axis

5 Error Integral

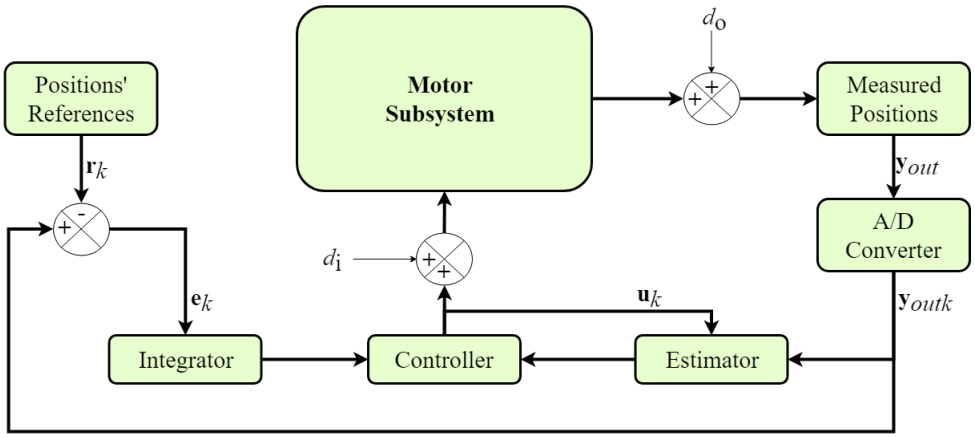

Figure 40: Controlled System's Structure with Controller, Estimator and Error Integral

The integral action is generally added in order to reduce the steady-state errors in a feedback control system. The integral action is carried out on the error, which is generally produced after comparison of the reference signal with the actual output. In our case, the error is $\mathbf{e}_k = \mathbf{y}_{\text{out}k} - \mathbf{r}_k$.

Now, a new state variable ("time integral" of the error) is introduced

$$\mathbf{x}_{\text{I}(k+1)} = \mathbf{x}_{\text{I}(k)} + \mathbf{e}_k = \mathbf{x}_{\text{I}(k)} + \mathbf{y}_{\text{out}k} - \mathbf{r}_k = \mathbf{x}_{\text{I}(k)} + \mathbf{C}\mathbf{x}_k - \mathbf{r}_k \tag{31}$$

Now, considering the augmented system, Eq (31) has the following look in matrix form

$$\mathbf{x}_{\text{I}(k+1)} = \begin{bmatrix}\mathbf{I} & \mathbf{C} & \mathbf{O}\end{bmatrix} \begin{bmatrix}\mathbf{x}_{\text{I}(k)} \\ \mathbf{x}_k \\ \hat{\mathbf{x}}_k\end{bmatrix} + \begin{bmatrix}-\mathbf{I}\end{bmatrix} \mathbf{r}_k \tag{32}$$

The control for the dynamics of the modified system, as required by the augmented system, can now been adjusted in the following fashion

$$\mathbf{u}_k = -\begin{bmatrix}\mathbf{K}_{\text{I}} & \mathbf{K}\end{bmatrix} \begin{bmatrix}\mathbf{x}_{\text{I}(k)} \\ \hat{\mathbf{x}}_k\end{bmatrix} \tag{33}$$

where, $\mathbf{K}_{\text{I}}$ is the discrete controller matrix for the error integral part of the augmented system. After taking into consideration the new control law, the full augmented system, together with all the states, will look like

$$\begin{bmatrix} \mathbf{x}_{\mathrm{I}(k+1)} \\ \mathbf{x}_{k+1} \\ \hat{\mathbf{x}}_{k+1} \end{bmatrix} = \begin{bmatrix} \mathbf{I} & \mathbf{C} & \mathbf{O} \\ -\mathbf{G}\mathbf{K}_{\mathrm{I}} & \mathbf{F} & -\mathbf{G}\mathbf{K} \\ -\mathbf{G}\mathbf{K}_{\mathrm{I}} & \mathbf{L}\mathbf{C} & (\mathbf{F}-\mathbf{G}\mathbf{K}-\mathbf{L}\mathbf{C}) \end{bmatrix} \begin{bmatrix} \mathbf{x}_{\mathrm{I}(k)} \\ \mathbf{x}_k \\ \hat{\mathbf{x}}_k \end{bmatrix} + \begin{bmatrix} -\mathbf{I} \\ \mathbf{O} \\ \mathbf{O} \end{bmatrix} \mathbf{r}_k \qquad (34)$$

I and **O** are identity and zero matrices, respectively, of proper orders. The main structure of the controlled system is already given by Figure 40. Figure 41 show the pole-zero map of the system with controller, estimator and integral action. Figure 42 show the step response of the same system. It can be observed that now there are no steady-state errors. The integral action has taken care of the errors and eliminated them. Some oscillations are observed on the non-diagonal elements, but those are well within the desired limit (0.05 mm, or 0.5 in PU scale). The sensitivities of the controlled system are given by Figure 43 and Figure 44. They show some responses to the disturbances. This shows that the conservatism could be eliminated. The maximum allowable absolute value for both of them is 3, which approximates to 9.5 dB. The maximum values for both the sensitivities are well within that limit. Therefore, if there are disturbances at the reference-to-system and system-to-output junctions, the controller will be able to restore stability back to the controlled system.

Figure 45 demonstrates the initial rotor lift-up dyanmics. Figure 45(a) and Figure 45(b) show the suspension current waveforms in d- and q-axes in absence of q-axis motor current when the system contains controller, estimator and integral action. It can be observed from the two figures that, there are oscillations in the suspension current waveforms initially. However, thet settle down quite quickly due to the damping property of the controller.

Figure 45(c) and Figure 45(d) present the responses of the rotor positions in x- and y-axes in absence of q-axis motor current for the same case. The oscillations in the rotor are observed, due to similar oscillations in suspension current waveforms. But these also settle down with the settling of the oscillations in suspension currents. The estimated positions nearly follow the actual positions and position references but there are still some error in the estimations. These errors, however, do not cause any instability in the system.

Figure 45(e) and Figure 45(f) show the simulated suspension forces' waveforms in x- and y-axes, respectively.

Figure 46 demonstrates the responses of the system to step change in input and starting of q-axis motor current. Figure 46(a) and Figure 46(b) show the suspension current waveforms in d- and q-axes when there is step change as well as when motor current is started. It can be observed from the two figures that, the step changes cause the suspension currents to ajdust in order to make the rotor follow its new references. The suspension currents exhibit a little bit of oscillation when q-axis motor current is started, but they settle down quite quickly and q-axis motor current do not have any influence on them any further.

Figure 46(c) and Figure 46(d) present the responses of the rotor positions for the same case. The rotor follows its references without any steady-state errors, as augured by Figure 42. The rotor position shifts slightly from its references when q-axis motor current is started, but that shift is well within allowable limit of 0.5 p.u. and the rotor also returns to its original position quite quickly. The q-axis motor current does not have any further influence on the rotor position.

Figure 46(e) and Figure 46(f) show the simulated suspension forces' waveforms in x- and y-axes, respectively.

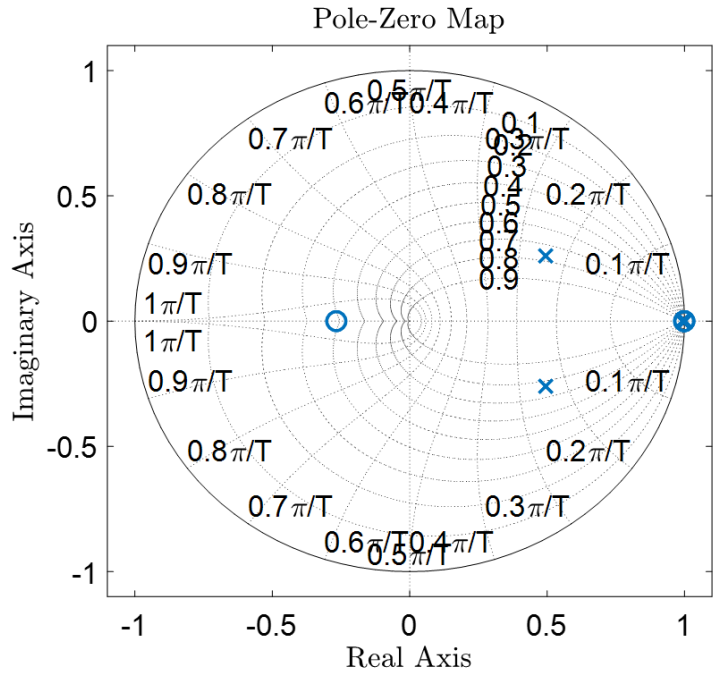

Figure 41: Pole-Zero Map of the System with Controller, Estimator and Integration

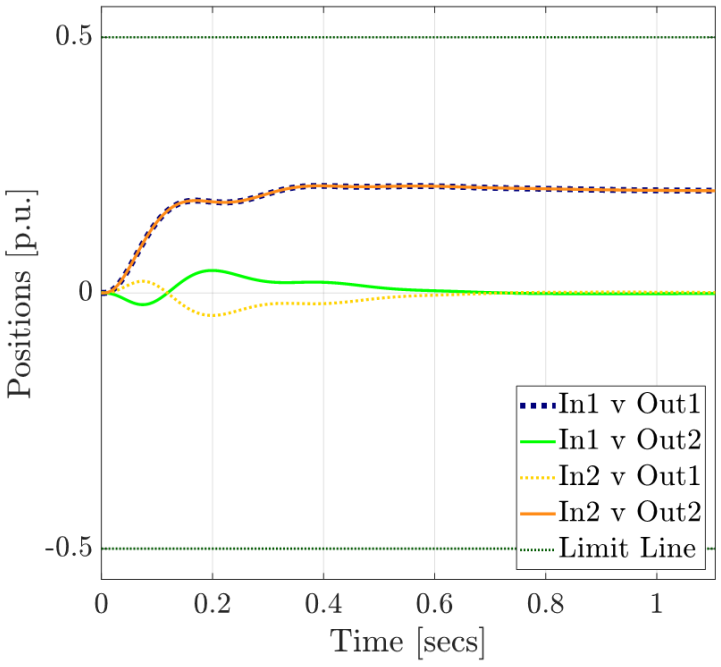

Figure 42: Step Response of the System with Controller, Estimator and Integration

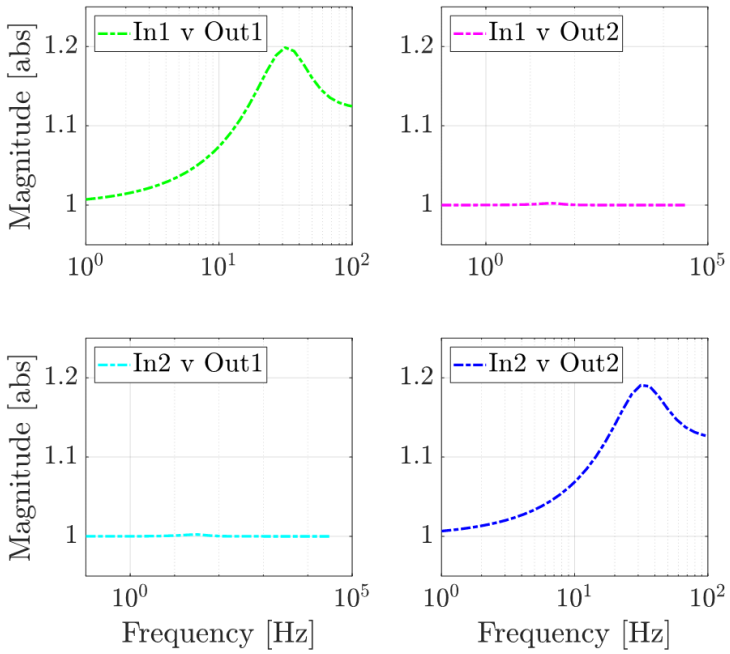

Figure 43: Reference-to-Error Sensitivity

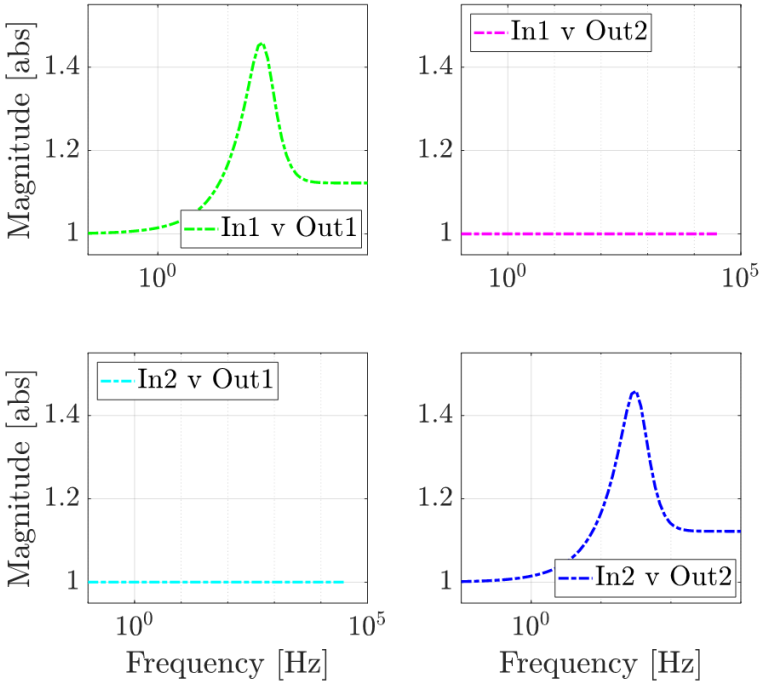

Figure 44: Output Disturbance-to-Output Sensitivity

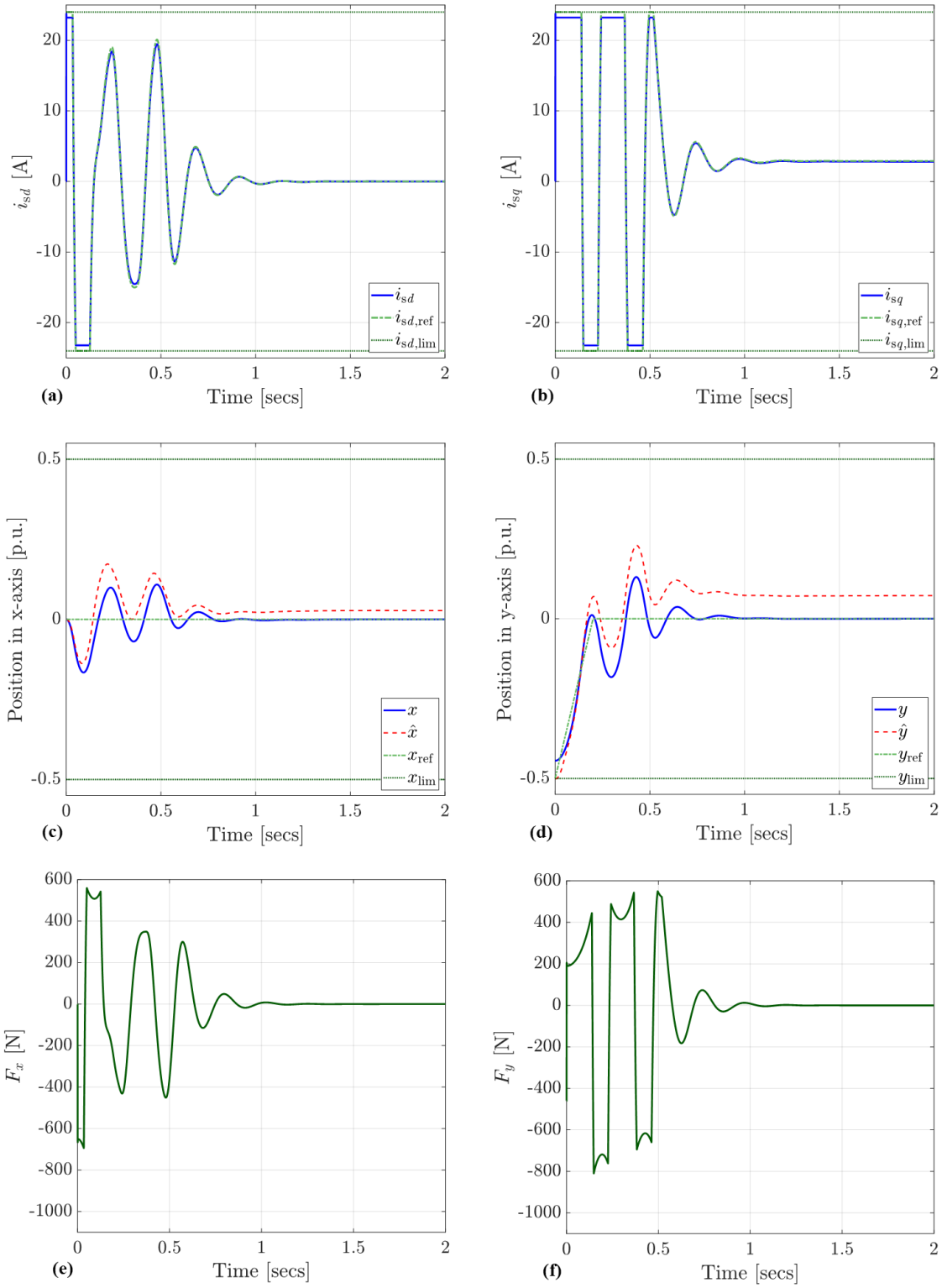

Figure 45: Rotor Lift-Up Dynamics – **(a)** Suspension current waveform in d-axis, **(b)** Suspension current waveform in q-axis, **(c)** x-axis rotor position, **(d)** y-axis rotor position, **(e)** Simulated suspension force waveform along x-axis, **(f)** Simulated suspension force waveform along y-axis

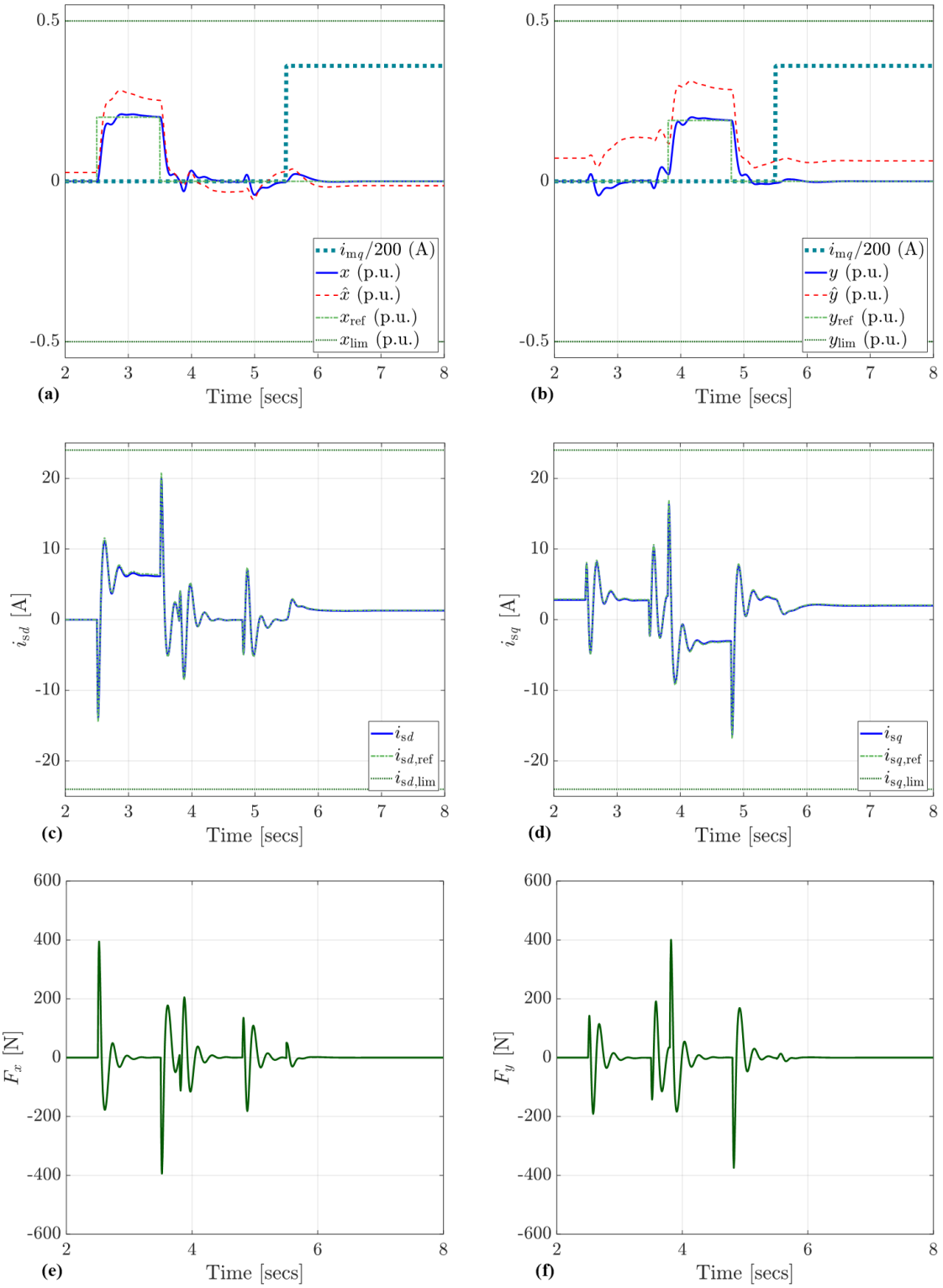

Figure 46: Step Change and Motor Current Dynamics – **(a)** x-axis rotor position, **(b)** y-axis rotor position, **(c)** Suspension current waveform in d-axis, **(d)** Suspension current waveform in q-axis, **(e)** Simulated suspension force waveform along x-axis, **(f)** Simulated suspension force waveform along y-axis

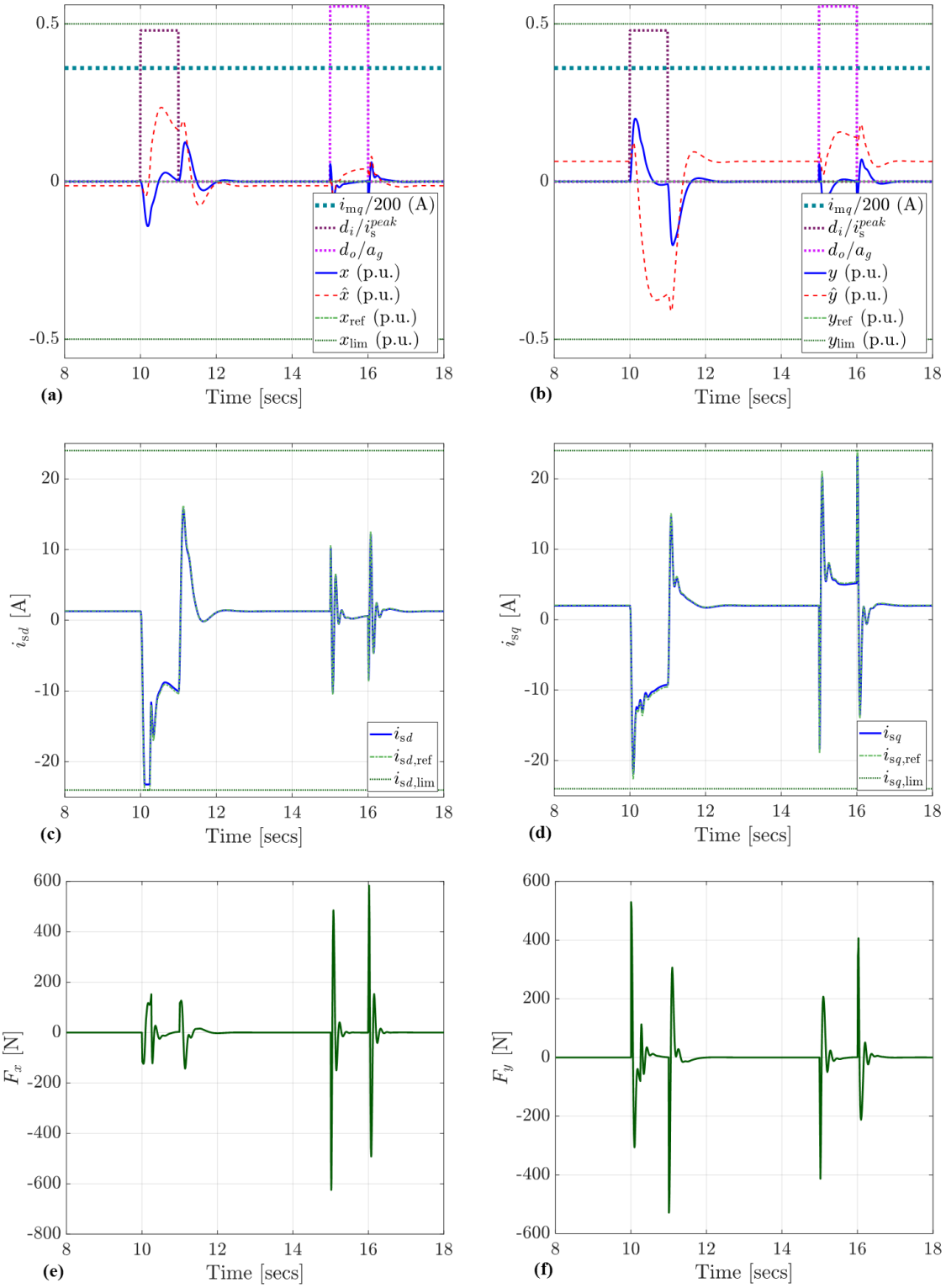

Figure 47: Step Input and Output Disturbances Dynamics – **(a)** x-axis rotor position, **(b)** y-axis rotor position, **(c)** Suspension current waveform in d-axis, **(d)** Suspension current waveform in q-axis, **(e)** Simulated suspension force waveform along x-axis, **(f)** Simulated suspension force waveform along y-axis

6 Stable Control Strategies

6.1 Comparison of the Two Stable Controllers

So far only two control strategies provided good responses for the system. They are controller and state-command control strategy and controller, estimator and integral control strategy. Here, the pros and cons of these two control strategies are discussed in detail. Table 2 presents the pros and cons for controller and state-command control strategy whereas, Table 3 does the same for controller, estimator and integral control strategy.

Table 2 – Pros and Cons of Controller and State-Command

Pros	• Output follows the reference pretty accurately • Oscillations are present, but they do not destabilize the system
Cons	• Outputs appear to be slightly over-damped

Table 3 – Pros and Cons of Controller, Estimator and Integral

Pros	• Output follows the reference pretty accurately • Oscillations are present, but they settle down pretty quickly
Cons	• Slight coupling between the control signals is visible from outputs

6.2 Ultimate Selection

Choosing the best between the two as the ultimate selection is going to be tough because both the control strategies have almost the same advantages. In order to

decide on the ultimate selection, the drawbacks will have to be taken into account. However, there is a catch: (i) state-command paths are generally preferred for those systems where the references do not change too much, (ii) error integral paths are generally preferred for those systems where output disturbances are expected to be present. For the system under investigation, both constant reference and anticipation of output disturbances hold true. So, in this case the ultimate selection will be quite a tricky one. It would be safe to assert that the system can be tried out with any one of these stable control strategies or perhaps with both of them, depending upon the type of application and the environment in which the system is functioning. If the application does not require the reference to be altered too often, controller and state-command control strategy is good to go with. Otherwise, if the operating environment forbodes disturbances at the output side of the system, control strategy with controller, estimator and integral would come in really handy here.

7 Conclusions

The thesis deals with the investigation of model-based control of levitation forces of bearingless interior permanent magnet motor by means of its suspension currents. The rotor needs to be kept levitated at the desired positions so that it is able to perform precisely under challenging operating environments for those applications which demand rotation of the rotor at high-speeds. The motor under investigation is capable of producing 100 kW power for high-speed applications in industrial pumps and compressors, for instance. Model-based control techniques have been investigated before, but not for any bearingless motor with 5-degrees-of-freedom (5-DOF). The point mass of the rotor is considered for the research investigation.

Five different control strategies, which include combination of controller, estimator, integral and state-command path, have been developed and tested for the system under investigation. In order to develop these model-based control strategies the levitation forces in x- and y-axes of the rotor are expressed as a function of suspension currents, position stiffness and current stiffness. Thereafter, those forces are broken down into state-space models with velocities and positions in both x- and y-axes as states and only the positions in x- and y-axes as outputs. These state-space models are later used in order to derive the gains for controller, estimator, integral and state-command path. The rotor levitation control is then tested with the following control strategies: (i) controller only, (ii) controller and state-command path, (iii) controller and estimator, (iv) controller, estimator and state-command path, and (v) controller, estimator and integral. The step and frequency responses of each of the proposed control strategies are presented. The trajectories of the outputs and control signals are shown in order to describe and delineate their behaviours with respect to time.

Control strategies which involve controller and state-command path and controller, estimator and integral show relatively better results amongst the five control strategies developed for the levitated rotor system. They bear similar advantages. The only difference they have is in their drawbacks. The outputs for controller and state-command appear slightly overdamped. However, this overdamping does not hamper the overall stability of the system. For the controller, estimator and integral control strategy, the drawback lies in the fact that, slight coupling between the control signals is visible. But then again, the system does not become unstable because of the coupling. Depending upon whether reference is changing or the operating environment produces output disturbances, one or the other can be chosen for levitation purposes. The ultimate selection between the two is difficult if pros of each of them, are taken into consideration.

In the future, it would be really nice to find out the optimal control strategy when the rigid rotor model is taken into account. Furthermore, different references and operating environments could be simulated in order to find out the best between the two control strategies that are discussed above. It would be good to find out whether both of them work or only one of them works. The motor which is capable

of producing 100 kW power and rotating at 22000 rpm has been investigated. Hence, it would also be nice if levitation control of motors used for intense high-speed operations were also investigated. Having said that, investigations are possible if sufficient interest in this emerging field exists. With the advance of control theory and its applications, it would be safe to presume here that levitation control will become popular and related research work will become possible as well.

References

[1] MUNTEANU, G., BINDER, A., SCHNEIDER, T. 2011. Development and test of high-speed bearingless PM synchronous machines. *Elektrotechnik und Informationstechnik*. 128 (3): 75−80. doi: 10.1007/s00502-011-0810-1

[2] ZHOU, L., TRUMPER, D. L. 2017. Reluctance Force Magnetic Suspension Characteristics and Control for Cylindrical Rotor Bearingless Motors. *Journal of Dynamic Systems, Measurement, and Control*. 139 (3). doi: 10.1115/1.4035007

[3] SUN, X., CHEN, L., JIANG, H., et al. 2016. High-Performance Control for a Bearingless Permanent-Magnet Synchronous Motor Using Neural Network Inverse Scheme Plus Internal Model Controllers. *IEEE Transactions on Industrial Electronics*. 63 (6): 3479−3488. doi: 10.1109/TIE.2016.2530040

[4] JASTRZEBSKI, R. P. 2007. *Design And Implementation of FPGA-Based LQ Control of Active Magnetic Bearings*. PhD Thesis. Lappeenranta University of Technology.

[5] JASTRZEBSKI, R. P., JAATINEN, P., CHIBA, A., PYRHÖNEN, O. (2016). Efficiency of buried permanent magnet type 5kW and 50kW high-speed bearingless motors with 4-pole motor windings and 2-pole suspension windings. In: *15th International Symposium on Magnetic Bearings*, Kitakyushu, Japan, 3−6 Aug (pp. 1−8)

[6] JASTRZEBSKI, R. P., JAATINEN, P., SUGIMOTO, H., et al (2015). Design of a bearingless 100 kW electric motor for high-speed applications. 2015 18$^{\text{th}}$ International Conference on Electrical Machines and Systems, Pattaya, Thailand, 25−28 Oct (pp. 2008−2014)

[7] PYRHÖNEN, J., JOKINEN, T., HRABOVCOVÁ, V. (2014). *Design of Rotating Electrical Machines*. 2nd ed. Chichester: John Wiley and Sons.

[8] HENDERSHOT, J. R., MILLER, T. (2010). *Design of Brushless Permanent-Magnet Machines*. 2nd ed. München: Motor Design Books LLC.

[9] CHIBA, A., FUKAO, T., ICHIKAWA, O., OSHIMA, M., TAKEMOTO, M., and DORELL, D. G. (2005). *Magnetic Bearings and Bearingless Drives*. Amsterdam: Elsevier.

[10] BIN, L. (2015). Survey of Bearingless Motor Technologies and Applications. In: *International Conference on Mechatronics and Automation*. Beijing: IEEE, pp. 1983−1988.

[11] ASANO, Y., MIZUGUCHI, A., AMADA, M., et al. 2009. Development of A Four-Axis Actively Controlled Consequent-Pole-Type Bearingless Motor. *IEEE Transactions on Industry Applications*. 45 (4): 1378−1386. doi: 10.1109/TIA.2009.2023498

[12] ASAMA, J., NAKAMURA, R., SUGIMOTO, H., CHIBA, A. 2011. Evaluation of Magnetic Suspension Performance in a Multi-Consequent-Pole Bearingless Motor. *IEEE Transactions on Magnetics*. 47 (10): 4262−4265. doi: 10.1109/TMAG.2011.2158076

[13] SUGIMOTO, H., UEMURA, Y., CHIBA, A., et al. 2013. Design of homopolar consequent-pole bearingless motor with wide magnetic gap. *IEEE Transactions on Magnetics*. 49 (5): 2315−2318. doi: 10.1109/TMAG.2013.2243420

[14] GRUBER, W., BRIEWASSER, W., ROTHBÖCK, M., SCHÖB, R. T. (2013). Bearingless slice motor concepts without permanent magnets in the rotor. In: *International Conference on Industrial Technology*. Cape Town: IEEE, pp 259−265.

[15] RAO, J., HIJIKATA, W., SHINSHI, T. (2014). A permanent magnet free bearingless motor for disposable centrifugal blood pump. In: *Proceedings of the 14th International Symposium on Magnetic Bearings*.

[16] RECHEIS, M. N., SCHWEIGHOFER, B., FULMEK, P., et al. 2014. Selection of magnetic materials for bearingless high-speed mobile flywheel energy storage systems. *IEEE Transactions on Magnetics*. 50 (4). doi: 10.1109/TMAG.2013.2291938

[17] ITO, E., CHIBA, A., FUKAO, T. (1997). A measurement of VA requirements in an induction type bearingless motor. *Proceedings of the 4th International Symposium on Magnetic Suspension Technology*.

[18] SCHÖB, R. 2002. Centrifugal pump without bearings or seals. *World Pumps*. 2002 (430): 34−37. doi: 10.1016/S0262-1762(02)80218-8

[19] OKADA, Y., YAMASHIRO, N., OHMORI, K., et al. 2005. Mixed Flow Artificial Heart Pump With Axial Self-Bearing Motor. *IEEE/ASME Transactions on Mechatronics*. 10 (6): 658−665. doi: 10.1109/TMECH.2005.859827

[20] YANG, S., HUANG, M. 2009. Design and Implemetation of a Magnetically Levitated Single-Axis Controlled Axial Blood Pump. *IEEE Transactions on Industrial Electronics*. 56 (6): 2213−2219. doi: 10.1109/TIE.2009.2017095

[21] REICHERT, T., NUSSBAUMER, T., KOLAR, J. W. 2012. Beringless 300-W PMSM for Bioreactor Mixing. *IEEE Transactions on Industrial Electronics*. 59 (3): 1376−1388. doi: 10.1109/TIE.2011.2126532

[22] WARBERGER, B., KAELIN, R., NUSSBAUMER, T., KOLAR, J. W. 2012. 50-N · m/2500-W Bearingless motor for High-Purity Pharmaceutical Mixing. *IEEE Transactions on Industrial Electronics*. 59 (5): 2236−2247. doi: 10.1109/TIE.2011.2161657

[23] SEVERSON, E., MOHAN, N. (2017). Bearingless motor System Design for Industrial Applications. In: *2017 IEEE International Electric Machines and Drives Conference*. [online] Miami: IEEE. Available at: https://ieeexplore.ieee.org/document/8002373/ [Accessed 09 May 2018].

[24] FRANKLIN, G. F., POWELL, J. D., WORKMAN, M. L. (1998). *Digital Control of Dynamic Systems*. 3rd ed. Menlo Park: Addison Wesley Longman, Inc.

[25] BRYSON, A. E., HO, Y. (1975). *Applied Optimal Control*. New York: Taylor and Francis Group.

[26] ASSIMAKIS, N., ADAM, M. 2013. Kalman Filter Riccati Equation for the Prediction, Estimation, and Smoothing Error Covariance Matrices. *ISRN Computational Mathematics*. 2013: 1−7. doi: 10.1155/2013/249594